The Meteoritical Society

Meteoritics & Planetary Science 43, Nr 1/2, 187–213 (2008)
Abstract available online at http://meteoritics.org

Chemical composition and heterogeneity of Wild 2 cometary particles determined by synchrotron X-ray fluorescence

A. LANZIROTTI[1], S. R. SUTTON[1, 2], G. J. FLYNN[3], M. NEWVILLE[1], and W. RAO[4]

[1]Center for Advanced Radiation Sources, University of Chicago, Chicago, Illinois 60637, USA
[2]Department of Geophysical Sciences, University of Chicago, Chicago, Illinois 60637, USA
[3]Department of Physics, State University of New York at Plattsburgh, Plattsburgh, New York 12901, USA
[4]Savannah River Ecology Laboratory, University of Georgia, Aiken, South Carolina 29808, USA
*Corresponding author. E-mail: Lanzirotti@uchicago.edu

(Submitted 30 May, 2007; revision accepted 13 October 2007)

Abstract–Seven cometary dust particle tracks in Stardust aerogel were studied using synchrotron X-ray fluorescence methods at the National Synchrotron Light Source (NY) and Advanced Photon Source (IL). Elemental maps were produced for each of the tracks and elemental abundances for 156 individual fragments within these tracks were determined. Whole-track elemental abundances were inferred by summing the elemental masses for the fragments in each track and scaling by the ratio of total Fe in the map and total Fe in the fragments. In general, whole-track and terminal-particle abundances are dissimilar. The total Fe masses ranged from 4 to 2200 pg, corresponding to impactors in the size range of 2.7 to 22 μm if Fe abundances are equal to the chondritic value. Systematic variations in element abundance with fragment distance from the aerogel entry point were generally subtle but were pronounced in one track (C2115,19). In this track, Zn/Fe was about three orders of magnitude higher at the top, Cr/Fe was two orders of magnitude higher at the bottom, and S was relatively uniform. Compositional convergence data showed that typically analysis of ~10 fragments was needed to reach convergent whole-track abundance. Zinc was an exception, showing non-convergent profiles and steps due to the presence of rare, high-Zn fragments. The resulting whole-track elemental abundances show diverse patterns that are generally chondritic (i.e., within a factor of three of CI abundances) with some exceptions, notably depletions in S and enrichments in the moderately volatile elements Cu, Zn, and Ga. Enrichments in large ion lithophile elements relative to Fe were observed in one track. Correlation matrices showed several strong elemental correlations, notably selenium associated with sulfur (sulfides), a ubiquitous correlation of the first-row transition metals Cr, Mn, and Fe attributed to the presence of pyroxene, and enrichments of gallium associated with calcium, likely affiliated with Mg-Al glass.

INTRODUCTION

A critical goal of NASA's Stardust mission is to provide information about the chemical composition of comets and their constituent components, including interstellar grains. An evaluation of the major- and trace-element composition of Wild 2 grains can be used to evaluate whether the mean composition of this material is chondritic and if chondrites are reasonable proxies of true solar abundances. These data can also provide insight into the chemical histories of this material.

Composition studies have been conducted on interplanetary dust particles (IDPs) collected from the stratosphere (Schramm et al. 1989), some of which are thought to be of cometary origin. Bulk composition analyses using synchrotron X-ray microprobes on IDPs (typically 1 ng) show generally "chondritic" abundance patterns with enrichments in moderately volatile elements (Flynn et al. 1996). The suggestion has been that the contents of such elements in primitive solar system solids may have been underestimated based on the compositions of CI meteorites. Another interesting conclusion from the IDP work is that the compositions of these particles do not vary widely from chondritic abundance (Flynn and Sutton 1990). This is thought to be due largely to the preferential production of fine-grained particles in this size range by parent body impacts (Flynn and Durda 2004).

The cometary particles collected by Stardust impacted the silica aerogel capture media at velocities of ~6 km s^{-1}, resulting in disaggregation of the grains along tracks of varying size and morphology. It has been estimated that up to 90% of the incoming particle mass resides along the aerogel penetration tracks (Flynn et al. 2006). There is also evidence that individual impacting grains experienced heating effects on capture that, in extreme cases, resulted in melting of aerogel and some particle components (Zolensky et al. 2006; Chi et al. 2007). These effects can result in a complex heterogeneous distribution of chemical components along the capture track. Additional complexities arise in evaluating potential trace-element contamination from the aerogel capture media. Since many analyses in the future will be conducted on individual fragments extracted from the capture tracks, an evaluation of this chemical heterogeneity is critical.

This physical disruption complicates efforts to reconstruct the bulk chemical composition of the impacting grains, but also offers an opportunity to study the nature of the grain components through analysis of the individual constituent fragments. Several questions can be addressed with such data, such as whether there is a correlation between fragment heterogeneity and whole track composition and/or track morphology. Such comparisons might tell us something about the grain size of various cometary components. For example, are volatile element-bearing components concentrated in smaller grains than refractory ones?

Estimates of bulk-track composition based on compositional mapping were obtained during the Stardust Preliminary Examination (PE) using synchrotron microprobe and TOF-SIMS analyses on aerogel tracks and SEM/EDS analyses on impact crater residues in Al foil (Flynn et al. 2006). This work concluded that:

- The particles are chemically heterogeneous at the largest size scale analyzed (~180 ng).
- The mean composition is consistent with that of CI meteorites to 35% for Mg, Si, Mn, Fe, and Ni and 60% for Ca and Ti.
- The moderately volatile elements Cu, Zn, and Ga appear to be enriched.

The purpose of this paper is to provide some insight into the chemical heterogeneity of fragments dispersed within individual tracks. We present long dwell-time elemental analyses of 156 individual fragments distributed along seven different capture tracks in aerogel keystones.

These data were collected using X-ray microprobes at the Advanced Photon Source and the National Synchrotron Light Source. Using energy dispersive synchrotron X-ray fluorescence (SXRF) analysis, it is possible to obtain full quantitative composition analyses on the micrometer-sized samples collected by the Stardust spacecraft for major and trace elements with, in many cases, sub-femtogram detection sensitivity. Another significant advantage of SXRF for this purpose is that these analyses can be conducted in situ within the aerogel capture media, foregoing the necessity of particle extraction and its associated risks of elemental contamination and fragment loss.

The data demonstrate that the disrupted fragments are chemically and mineralogically heterogeneous at the 10 μm scale, so that individual fragment analyses are typically nonrepresentative of the impactor composition. However, as a population, fragments from individual tracks often show similarities in the ratio of elements, likely reflecting the multiple component mineralogy of the fragments at the micrometer scale. While this is an important constraint on the nature of the fine-scale minerals and components of the Wild 2 comet, this also highlights the potential complexity of how best to reconstruct the bulk composition of the impacting particle, from the heterogeneous deposition of material of various sizes along the entry track.

STARDUST SAMPLES

SXRF data are presented here for seven Stardust tracks. All were in the form of aerogel keystones produced either at NASA-JSC or the University of California (Berkeley).

- C2115,19: A carrot-type track 890 μm in length with a single terminal particle. X-ray fluorescence (XRF) maps indicate the terminal particle contains 10% of the total Fe mass in the track. The whole-track abundance pattern determined using the fragment sum method (Flynn et al. 2006; SOM) and normalizing to Fe and CI (Fig. 4a) shows a generally chondritic pattern with depleted Ca and Ge, and enriched Zn and Ga.
- C2115,20: A carrot-type track 900 μm in length. The terminal particle contains 16% of the total Fe mass. The whole-track abundance pattern (CI- and Fe-normalized; Fig. 4b) shows a generally enriched composition with enrichments in most elements except Ca and Ni. The track is dominated by low-Ca pyroxene (Zolensky et al. 2006).
- C2115,21: A carrot-type track 900 μm in length. The terminal particle contains 42% of the total Fe mass. The whole-track abundance pattern (CI- and Fe-normalized; Fig. 4c) shows a generally chondritic composition with depletion in S and enrichments in Zn and Ga.
- C2115,22: A bifurcated carrot-type track 3900 μm in length. The main terminal particle contains 70% of the total Fe mass. The whole-track abundance pattern (CI- and Fe-normalized; Fig. 4d) shows large depletions in S, Ni, and Ge, and large enrichment in Ga. The track is dominated by olivine with Cu-Fe and Fe-Zn sulfides (Zolensky et al. 2006).
- C2044,12: A carrot-type track 1500 μm in length. The terminal particle contains 81% of the total Fe mass. The whole-track abundance pattern (CI- and Fe-normalized; Fig. 4e) shows a generally depleted composition with depletions in S, Ca, Mn, and Zn.

- C2044,7: A carrot-type track 1500 μm in length. No distinct terminal particle was identified in this track. The whole-track abundance pattern (CI- and Fe-normalized; Fig. 4f) shows a generally chondritic composition with S depletion and Cu enrichment.
- C2027,48: A bulb grading into a carrot-type track 2100 μm in length. The bulb and track were mapped separately as individual pieces of aerogel. Additionally, the bulb was dissected in two, exposing the inner surface of the track. Each bulb half was analyzed individually. The terminal particle contains 11% of the total Fe mass. The whole-track abundance pattern (CI- and Fe-normalized; Fig. 4g) shows a generally chondritic composition with S depletion and Zn enrichments.

ANALYTICAL METHODS

XRF maps and spot XRF analyses were obtained using the undulator-based microprobe at Sector 13 (GeoSoilEnviroCARS) at the Advanced Photon Source (APS), Argonne National Laboratory, and bending-magnet-based microprobe at beamline X26A at the National Synchrotron Light Source (NSLS), Brookhaven National Laboratory (Sutton et al. 2002, 2004). Both instruments used a Si (111) monochromator and Kirkpatrick-Baez microfocusing mirrors (KB) (Kirkpatrick and Baez 1948; Eng et al. 1995, 1998; Yang et al. 1995). The KB system consisted of two mirrors (100 mm in length) in tandem, one oriented horizontally and one oriented vertically. Each mirror, a highly polished, flat, single crystal of silicon coated with several hundred Å of Rh, was dynamically bent to an elliptical shape using a mechanical bender. A 300 × 300 μm X-ray beam incident on the mirror pair was focused by reflection to ~3 × 3 μm (APS) and ~5 × 8 μm (NSLS). XRF spectra were collected using a Vortex-EX silicon drift detector utilizing digital signal processing electronics with an energy resolution of ~130 eV at Mn K_α. Incident-beam energies of 16.5 and 23 keV were used at NSLS and APS, respectively. Maps were acquired by rastering the sample in the X-ray beam with 3 and 5 μm steps for the APS and NSLS, respectively. Dwell times were typically 0.5 and 2 s (APS and NSLS, respectively). Total mapping times were typically several hours per track. In addition, longer dwell spot XRF analyses (typically 5 to 10 min) were obtained on spots along the track with a high count rate (typically a high Fe K count rate) in order to increase the number of detectable elements.

One of the original goals of this study was to reconstruct the bulk chemical composition of the impacting grain. Two approaches were taken: integration of XRF maps and summation of individual XRF spectra on the most massive fragments. In the former approach, full XRF spectra were saved at each analysis pixel in the map of the entire track and all the spectra were summed to produce a whole-track spectrum. A portion of the map far from the track and showing no obvious signals from comet dust was then summed to produce an aerogel background spectrum. The whole-track and aerogel spectra were then subtracted using total pixels summed in each for normalization. One of the advantages of this background subtraction approach is that the defined aerogel spectrum includes elemental hot spots that are known to be present in the material. In addition, identification of aerogel pixels within the track is not required. The only assumption is that the total elemental masses of contaminants within the map region was not altered by the impact event, a reasonably good assumption even though these contaminating atoms were undoubtedly redistributed locally. The net, whole-track XRF spectrum was then fit using a Gaussian-based routine, and the net peak areas converted to masses using comparable measurements on SRM thin film standards 1832/1833. NRLXRF (Criss 1977) was used to make small self-absorption corrections and extrapolate sensitivities to elements not present in the SRMs. Abundance patterns were produced by normalizing the element masses to Fe and the concentration of that element in the CI meteorites (Anders et al. 1989). We also obtained quantitative analysis in this way for some "trackless" flight aerogel from cell C2054 to provide independent compositional data on impurities in the flight aerogel.

The short dwell time per pixel required for the maps to complete within a reasonable period of time plus the large amount of aerogel present in the maps meant some elements at low abundance were not adequately detected. For optimal detection sensitivity, long dwell time spectra on "hot-spots" were collected and fit individually and elemental masses computed for each as above. This approach is the focus of this paper, although admittedly this is not optimal in detecting diffuse components dispersed at the margins of tracks. These fragments were identified principally by high Fe intensity (i.e., they represented the high-Fe K_α intensities in the maps) and were selected to provide representative material along the entire track lengths. Some fragments were also included that yielded high intensities in the other maps (notably, Ni and Zn). Aerogel background subtractions for these single point analyses were generally done by subtracting a single point analysis approximately 100 μm away from the track to represent the composition of the aerogel matrix. "Blank" analyses of this kind showed generally good reproducibility. The energy dispersive spectrum of the aerogel background was then scaled to correct for any differences in incident beam intensity and dwell time relative to the fragment analysis.

Calculated elemental masses and abundances include 1σ random errors (precision), which account for uncertainties associated with counting statistics and spectral fitting, including uncertainties in aerogel spectrum subtraction, net background subtraction, and peak fitting. We generally omit statistical error bars in the figures presented here since measurement uncertainties are generally small compared to the large inter- and intra-track variations.

There are two principal potential sources of systematic error in the particle analyses. First, the SRM thin film standards have elemental concentration accuracies of about 10%. There is also the potential error associated with extrapolation of these sensitivity results to elements not present in the standards, a potential uncertainty which we estimate at about 10%. Second, the aerogel background subtraction procedure can systematically over- or underestimate the aerogel contribution to the particle spectra, primarily because the background spectra used are obtained at adjacent locations. Our aerogel spectra typically are equivalent at the 10% level. Thus, for elements with fluorescence energies greater than that of the Ca K_α emission line, where self- and aerogel absorption is negligible, the overall potential systematic errors in the particle masses are likely to be less than about 20% (since different systematic errors are not be expected to be in the same direction).

There is an additional potential source of systematic error in S and Ca analyses due to the uncertain absorption by overlying aerogel (uncorrected in the present work). If we assume a maximum keystone thickness of 300 μm of SiO_2 with a density of 0.02 g cm^{-3}, the fluorescence half-path is ~200 μm in our 45° geometry and the transmission is 0.60 for sulfur K_α and 0.87 for Ca K_α, i.e., absorption factors of 40% and 13%, respectively. Thus, realistically, the S and Ca masses could be underestimated by up to factors of 40% and 13%, respectively.

A total of 156 individual fragments were analyzed in this way: C2115,19 (23 fragments); C2115,20 (13 fragments); C2115,21 (17 fragments); C2115,22 (24 fragments); C2044,12 (18 fragments); C2044,7 (6 fragments); and C2027,48 (55 fragments). All seven tracks were analyzed at NSLS with a 16.5 keV beam and no detector filtering, which provided data for elements between S and Ga. The four C2115 tracks were subsequently analyzed at the APS with a 23 keV beam. No detector filtering was used for C2115,19, providing data for elements between S and Zr. A 70 μm thick Al detector filter was used for C2115, 20, 21, and 22, providing data for elements between Cr and Zr. The Al filter was used to suppress Fe K_α fluorescence and thereby enhance the sensitivities for high-Z elements. The NSLS and APS elemental masses were combined for each fragment analyzed with both instruments (10 fragments out of the total of 156 analyzed) to produce a single composition. In these combined data sets, S and Ca from the NSLS spectra were used; Cr, Mn, Fe, Ni, Cu, Zn, and Ga were averaged; and the APS data for Ge, Se, Br, Rb, Sr, Y, and Zr were used. For the averaged elements, the NSLS and APS mass results are typically within ~30% of the average values with even closer agreement for the abundance values.

To compute the bulk chemical composition of the impacting parent particle, these elemental masses were then summed to produce whole-track masses and abundances (Flynn et al. 2006). In some cases it was not possible to determine the mass of an element in the analysis due to detector filtering (preventing detection of light elements) or incident beam energy (preventing detection of heavy elements). These values are indicated as "nd," or "not determined." For an element containing fragments with nd values, the whole-track masses and abundances were estimated in the following way: the sum of all the "non-nd" masses for that element was divided by the sum of the Fe masses for just those non-nd particles, and this ratio was divided by the nominal CI Fe-normalized ratio for that element. This yields the CI-Fe normalized abundance for that element using just the particles that have data for that element. The whole-track mass for that element was then obtained by multiplying the "all particle Fe total mass" by the abundance ratio for that element. This approach basically assumes that the abundance ratio for the particles with nd is the average of the other particles in the track for which there are data.

The reported whole-track elemental masses were multiplied by a track-specific scaling factor, required because only a fraction of the total track was analyzed, taken to be the ratio of the Fe mass in the summed analyses and that in the map. This factor was between 2 and 9 but was 21 for C2115,19, a highly dispersed track. The use of this scaling factor assumes that the average composition of the analyzed cometary material is the same as that for all the cometary material in the track. This assumption will be most valid for tracks produced by fine-grained aggregates and less valid for those dominated by large mineral grains.

To evaluate the heterogeneity and elemental correlations in the Stardust tracks, we applied several statistical treatments to the individual fragment data. Primarily we have approached this evaluation by producing correlation plots for selected element pairs and correlation matrices for all elements detected. These data are expected to reveal the degree of correlation between elements in the cometary dust and provide insight into the hosts of these elements.

RESULTS AND DISCUSSION

Aerogel Inorganic Impurities

Some of the trace elements analyzed by SXRF require correction for inorganic contaminants present in the aerogel, accomplished here by subtracting aerogel spectra. Even when isolated in a thin (~200 to 300 μm thick) keystone, the aerogel in the volume occupied by the track produced by an ~10 μm impactor (mass ~1 ng) weighs ~1 μg, so even ppb contamination by an element is significant for that element present in the particle at the ppm level. Tsou et al. (2003) provide a comprehensive bulk analysis of inorganic contents on the flight batch aerogel by ICP/MS, but did not evaluate contaminant heterogeneity. The heterogeneity of

Table 1. Flight aerogel impurity contents.

Element	Tsou et al. (ppm)	C2054 mean (ppm)	C2054 max (ppm)	Std. dev.	% pixels > 3σ
Ca	5.20	7.52	98	6.14	4
Fe	1.80	1.02	1335	0.64	3
Ni	0.09	0.41	239	0.26	2
Cu	0.18	0.85	44	0.49	3
Zn	1.30	3.15	55	1.63	2

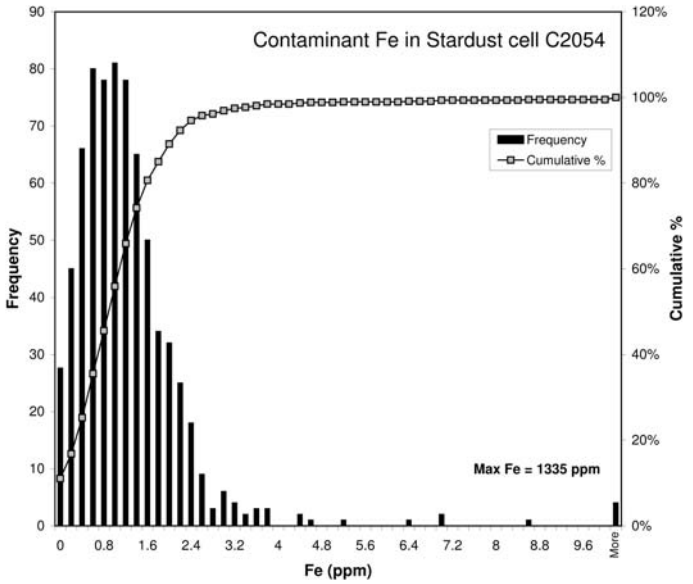

Fig. 1. Abundance histogram for contaminant Fe from a 3.25 mm × 6.25 mm section of flight aerogel cell C2054. Shown are pixel frequencies for Fe abundance up to 10 ppm. All pixels with abundance greater than 10 ppm (up to a maximum measured Fe abundance of 1335 ppm) are grouped in the "More" bin. Also shown is the cumulative percentage of pixels beginning with the smallest bin. The mean value of a normal distribution fitted to the data was 1.0 ppm with a standard deviation (σ) of 0.64 ppm (Table 1). Three percent of the pixels lie above the mean + 3σ (3.0 ppm).

contaminants is potentially problematic in attempting to correct SXRF data collected in situ within the aerogel capture media. We evaluated the magnitude of potential heterogeneities by compositionally mapping a 3.25 mm × 6.25 mm × 2 mm thick section of flight aerogel from cell C2054. Elemental abundance was calculated as described above and then converted to units of concentration by measuring X-ray transmission through the sample and calculating an effective thickness for the aerogel assuming a mass absorption coefficient. The mean concentrations of elements that were detectable as contaminants are presented in Table 1 and compared to ICP-MS data from Tsou et al. (2003). In general there is good agreement between the two sets of analyses, with bulk concentrations of Fe, Ni, and Cu of about 1 ppm or less. Both sets of analyses show Ca and Zn concentrations of several ppm, and the SXRF analysis of Zn is a factor of about 2.5 higher in concentration. Spatially resolved SXRF mapping demonstrates that all these elements display a similar distribution of elemental abundance that approximates a normal distribution at low concentrations (portion of the distribution containing nearly all the pixels) with a long tail to high concentrations (see, for example, the Fe histogram in Fig. 1). Hot spots were defined to be those pixels that lie at higher concentrations than the mean of the "normal" distribution plus 3 times the standard deviation. The percentage of hot spots in the element maps was 2–4% for Ca, Fe, Ni, Cu, and Zn. These localized single pixel hot spots can have metal abundances elevated above the bulk abundances by roughly a factor of 10 for Ca, Zn, and Cu, and a factor of 1000 for Fe and Ni.

It is important to consider the potential effect of these hot spots on the fragment abundances. The flight aerogel piece analyzed here was about 10 times as thick as the typical keystone (2 mm versus 0.2 mm), so the probability that a hot spot may be intimately associated with a cometary dust fragment is on the order of a permil. Since we analyzed 156 fragments, we expect no analyses to be contaminated in this way. It is also conceivable that these contaminant hot spots could be mistaken for cometary fragments. However, a typical keystone track XRF map consisted of ~10^3 pixels, suggesting that only one of the pixels in each map is likely to have been a contaminant hot spot.

Track Characteristics

Since most of the major minerals in meteorites and IDPs contain some Fe, Fe was used as a proxy to map the spatial distribution of the cometary material along the tracks. Figure 2 shows the Fe maps of all seven tracks in this study. The most notable feature is that fragments of the impactor are distributed along the entire length of each track. All the tracks examined (with the possible exception of C2044,7) have one or more remnants at the furthest extent of the track, so-called "terminal particles." The extent of the fragmentation varies from track to track. As mentioned above, the fractions of material remaining in the main terminal particles of each track varied from 10 to 70%. There appears to be a correlation between this factor and the distribution of matter in the track. Tracks with high fractional mass in the terminal particle tend to have the majority of the non-terminal mass concentrated close to the entry point, e.g., C2115,22 (Fig. 2). Those with low mass terminal particles tend to have material more uniformly distributed along the track, e.g., C2115,19 (Fig. 2). This suggests that the impactors of the former are principally composed of large crystals that easily shed adhering fine-grained material, whereas the latter are those lacking such large crystals.

Whole-Track Compositions

The measured elemental masses for the fragments are presented in Tables 2a–g. Each table shows the elemental masses (femtograms) for each fragment analyzed in the track. Values shown in italics are upper limits; these generally correspond to ~10 ag. In cases where an element in one or more of the fragments was undetected and is reported as an upper limit (italics), the whole-track mass shows two values. The first value was computed assuming the masses of the elements with upper limits are equal to the upper limits. The second value was computed assuming the masses of the elements with upper limits are equal to zero. These two values represent the range of possible whole-track values.

The validity of the "fragment summation" approach to determining whole-track compositions was tested by performing an "integrated map" analysis on track 19 for comparison. Figure 3 shows a comparison of abundance patterns obtained using these two different methods for the limited number of overlapping elements (from Flynn et al. 2006, supplemental information). The results are consistent at the 25% level for Mn, Ni, and Zn. Chromium and Cu show differences of about a factor of two. Such differences may result from the hot spot technique, analyzing a smaller fraction of the total material than the mapping method. These results provide evidence for the level of inaccuracies associated with integrating a subset of the track material.

The estimated total Fe mass for the seven tracks ranged from 4 to 2200 pg. The size of the impactors can be estimated by assuming the impactors were spheres of density 2 g cc^{-1} with Fe concentrations equal to CI. In this case, these Fe masses correspond to impactor diameters from 2.7 to 22 μm.

The abundance patterns (Fe and CI normalized) for whole tracks and terminal particles are shown in Figs. 4a–4g. Vertical lines on the whole-track patterns represent the range of possible values for elements for which the masses of one or more fragments were upper limits (dual whole-track values in Tables 2a–2g). The horizontal line at "1" represents the CI abundance pattern. As can be seen, the whole-track abundances show significant deviations from the CI abundances. Track C2115,19 shows a generally horizontal pattern with the average value around CI, but with minima and maxima extending to a factor of 10 from CI. Notable depletions are in Ca and Ge. The moderately volatile elements Zn, Ga, and Se are enriched. Track C2115,20 shows a generally increasing pattern with atomic number with enrichments in most elements except Ca, Ni, and Ge. Track C2115,21 shows a horizontal pattern analogous to that of C2115,19 with enrichments of Zn and Ga but with "normal" Se. Sulfur is also depleted as is Ge but Ca is "normal." Track C2115,22 shows a highly fractionated pattern with a large enrichment in Ga and depletions in S, Ni, Cu, Ge, and Sr. This is a pattern one might expect from a track produced by a large fractionated crystal and is consistent with the observation that the terminal particle is dominated by reversely zoned olivine (Zolensky et al. 2006). Track C2044,12 is depleted in S, Mn, and Zn. Track C2044,7 is the closest to a CI abundance pattern of the seven tracks, with a depletion in S and slight enrichment in Cu. Track C2027,48 is comparable to C2115,21 but with a smaller Ga enrichment.

Although none of the patterns are identical, C2115,19, C2115,21, and C2027,48 are fairly similar in composition, characterized by enrichment in Cu and Zn. Two out the three also have S depletion and Ga enrichment. C2044,12 and C2044,7 show the closest to CI abundance of the group. C2115,20 and C2115,22 have unique patterns, the former showing enrichments in large ion lithophiles (Rb, Sr, Y, Zr) and the latter yielding a highly fractionated pattern.

A comparison of the whole-track and terminal-particle abundance patterns (Figs. 4a–4g) demonstrates that the compositions of the terminal particles are typically significantly different from those of the whole tracks, and by extension, those of the impactors. In general, terminal particles show more depleted patterns than whole tracks, although this is not strictly true. For example, the C2115,19 terminal particle is depleted in many elements relative to the whole track. However, Cr, Mn, Fe, and Se are basically equivalent in the two. The greatest fractionation, about four orders of magnitude, is seen for

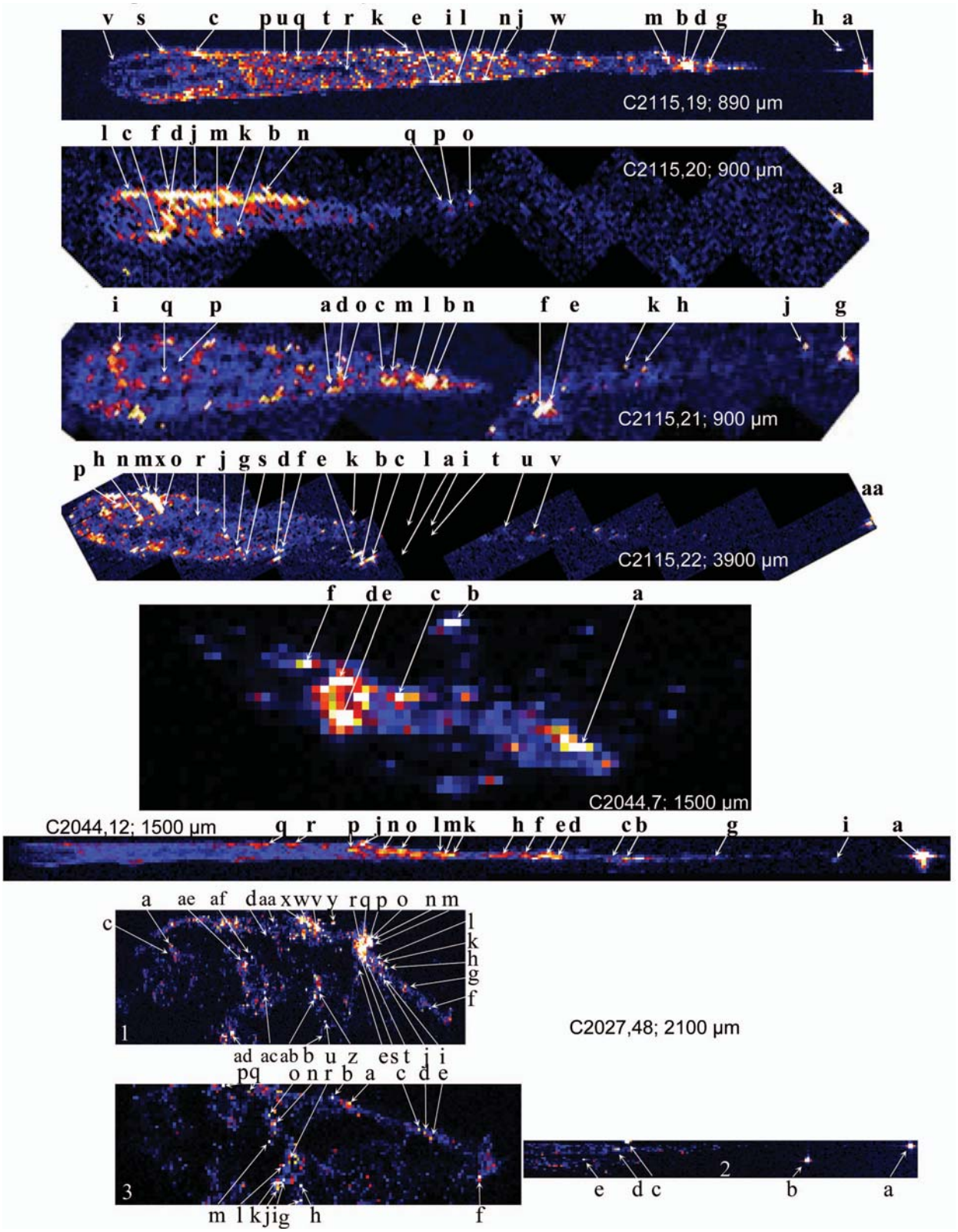

Fig. 2. a–g). Fe maps for the seven tracks in this study. Each map is annotated to indicate the locations of the 156 individual particles analyzed and reported in Tables 2a–g. Each Fe map is shown at a different scale; the actual length of each track (distance from entry point to farthest terminal particle) is shown. C2027,48 consisted of three aerogel pieces. Piece 2 is the narrow end portion of the track that was cut off from the upper portion. The upper bulbous portion was then sliced lengthwise to produce two half-bulbs, pieces 1 and 3.

Table 2a.

	Element mass (femtograms)															
	S	Ca	Cr	Mn	Fe	Ni	Cu	Zn	Ga	Ge	Se	Br	Rb	Sr	Y	Zr
Track C2115,19																
19a	700 (5)	5.4 (0.4)	292 (0.4)	52 (0.1)	7517 (1)	47 (0.1)	1.74 (0.10)	0.71 (0.10)	0.40 (0.10)	0.08 (0.11)	4.44 (0.09)	*0.05*	*0.02*	*0.02*	*0.01*	*0.01*
19b	132 (9)	2.9 (0.6)	9.33 (0.18)	2.19 (0.12)	378 (1)	28.7 (0.1)	0.53 (0.05)	7.95 (0.06)	0.09 (0.03)	*0.02*	0.10 (0.03)	*0.04*	*0.01*	*0.01*	*0.01*	*0.01*
19c	75 (7)	1.2 (0.5)	0.49 (0.13)	0.50 (0.10)	346 (1)	34.3 (0.1)	0.39 (0.04)	3.99 (0.05)	0.05 (0.03)	*0.02*	0.06 (0.02)	0.13 (0.02)	*0.01*	*0.01*	*0.01*	0.03 (0.02)
19d	105 (2)	9.1 (0.2)	3.46 (0.12)	1.77 (0.11)	238 (1)	15.1 (0.1)	0.57 (0.05)	2.10 (0.04)	0.24 (0.03)	*0.02*	0.05 (0.03)	0.02 (0.02)	*0.01*	*0.01*	*0.01*	*0.01*
19e	65 (8)	0.8 (0.6)	0.19 (0.13)	*0.10*	214 (1)	24.7 (0.1)	0.21 (0.04)	0.44 (0.04)	0.03 (0.03)	*0.02*	0.06 (0.02)	0.03 (0.02)	*0.01*	*0.01*	*0.01*	*0.03*
19f	51 (8)	0.6 (0.6)	0.41 (0.14)	0.15 (0.11)	226 (1)	8.3 (0.1)	0.12 (0.04)	1.95 (0.04)	0.03 (0.03)	*0.02*	0.06 (0.02)	*0.01*	*0.01*	*0.01*	*0.01*	*0.01*
19g	34 (4)	3.1 (0.3)	1.78 (0.07)	0.80 (0.06)	122 (1)	7.0 (0.1)	0.09 (0.02)	0.76 (0.02)	0.03 (0.02)	*0.02*	0.04 (0.01)	*0.01*	*0.01*	*0.01*	*0.01*	*0.01*
19h	123 (5)	9.2 (0.3)	53.8 (0.2)	20.1 (0.1)	369 (1)	8.9 (0.1)	0.31 (0.02)	0.29 (0.02)	0.05 (0.02)	*0.02*	0.09 (0.01)	*0.01*	*0.01*	*0.01*	*0.01*	*0.01*
19i	26 (8)	*0.6*	0.17 (0.13)	0.17 (0.10)	132 (1)	3.6 (0.1)	0.06 (0.04)	1.40 (0.04)	0.03 (0.03)	*0.02*	0.04 (0.02)	*0.01*	*0.01*	*0.01*	*0.01*	*0.01*
19j	88 (4)	2.0 (0.3)	0.60 (0.08)	0.55 (0.06)	380 (1)	9.4 (0.1)	0.18 (0.02)	2.37 (0.02)	0.06 (0.02)	*0.02*	0.10 (0.01)	*0.01*	*0.01*	*0.01*	*0.01*	*0.01*
19k	82 (7)	0.9 (0.5)	0.90 (0.13)	0.58 (0.10)	300 (1)	15.2 (0.1)	0.27 (0.04)	5.79 (0.05)	0.05 (0.03)	*0.02*	0.08 (0.02)	*0.01*	*0.01*	*0.01*	*0.01*	*0.01*
19l	79 (4)	1.4 (0.3)	0.34 (0.08)	0.08 (0.06)	302 (1)	15.9 (0.1)	0.16 (0.02)	0.70 (0.02)	*0.02*	*0.02*	0.09 (0.01)	*0.01*	*0.01*	*0.01*	*0.01*	0.03 (0.01)
19m	26 (4)	0.3 (0.3)	0.87 (0.07)	0.29 (0.05)	81 (1)	4.0 (0.1)	0.06 (0.02)	0.95 (0.02)	0.02 (0.02)	*0.02*	0.02 (0.01)	*0.01*	*0.01*	*0.01*	0.02 (0.01)	0.02 (0.01)
19n	67 (4)	1.7 (0.3)	0.68 (0.07)	0.25 (0.06)	236 (1)	19.3 (0.1)	0.35 (0.02)	1.89 (0.02)	0.03 (0.02)	*0.02*	0.07 (0.01)	*0.01*	*0.01*	*0.01*	0.02 (0.01)	0.02 (0.01)
19p	41 (4)	1.2 (0.3)	0.20 (0.07)	1.68 (0.06)	90 (1)	8.8 (0.1)	0.30 (0.02)	16.4 (0.04)	0.04 (0.02)	*0.02*	0.05 (0.01)	0.04 (0.01)	*0.01*	0.02 (0.01)	0.02 (0.01)	0.05 (0.01)
19q	29 (4)	0.9 (0.3)	0.16 (0.07)	1.46 (0.06)	82 (1)	28.7 (0.1)	0.34 (0.02)	14.3 (0.04)	0.04 (0.02)	*0.02*	0.05 (0.01)	*0.01*	*0.01*	0.02 (0.01)	0.02 (0.01)	0.03 (0.01)
19r	17 (4)	0.5 (0.3)	0.13 (0.07)	0.30 (0.05)	46 (1)	24.7 (0.1)	0.20 (0.02)	6.70 (0.03)	0.02 (0.02)	*0.02*	0.03 (0.01)	*0.01*	*0.01*	*0.01*	0.02 (0.01)	0.03 (0.01)
19s	57 (4)	2.2 (0.3)	0.67 (0.07)	0.50 (0.06)	169 (1)	32.8 (0.1)	0.57 (0.02)	0.62 (0.02)	0.05 (0.02)	*0.02*	0.04 (0.01)	*0.01*	0.01 (0.01)	0.02 (0.01)	0.02 (0.01)	0.06 (0.01)
19t	58 (4)	1.3 (0.3)	0.15 (0.07)	1.84 (0.06)	147 (1)	68.7 (0.1)	0.43 (0.03)	11.7 (0.04)	0.04 (0.02)	*0.02*	0.09 (0.01)	*0.01*	*0.01*	*0.01*	0.02 (0.01)	0.04 (0.01)
19u	23 (4)	1.2 (0.3)	0.32 (0.07)	1.81 (0.06)	81 (1)	17.0 (0.1)	0.33 (0.02)	17.6 (0.04)	0.04 (0.02)	*0.02*	0.05 (0.01)	*0.01*	*0.01*	*0.01*	0.02 (0.01)	0.03 (0.01)
19v	*106*	10.5 (0.5)	0.59 (0.20)	0.90 (0.10)	11 (0.2)	1.1 (0.2)	1.61 (0.06)	136 (0.1)	0.79 (0.05)	nd	nd	nd	nd	nd	nd	nd
19w	113 (5)	6.4 (0.4)	2.85 (0.20)	1.80 (0.10)	335 (1)	60.2 (0.3)	2.59 (0.06)	2.63 (0.06)	0.48 (0.05)	nd	nd	nd	nd	nd	nd	nd
19x	145 (5)	7.0 (0.5)	3.03 (0.20)	2.11 (0.10)	375 (1)	16.6 (0.2)	1.38 (0.06)	5.85 (0.05)	0.55 (0.05)	nd	nd	nd	nd	nd	nd	nd
Whole track masses (21)	47,500 (510) 45,200 (510)	1480 (41)	7890 (10)	1950 (7)	258,000 (100)	10,600 (10)	270 (3)	5150 (3)	67 (2) 66 (2)	8.3 (2.0) 1.9 (0.4)	126 (2.0) 126 (2.0)	10.9 (2.0) 5.0 (0.8)	5.5 (2.0) 0.3 (0.4)	5.8 (2.0) 1.2 (0.7)	6.5 (2.0) 3.3 (1.2)	10.5 (2.0) 7.4 (1.3)
Whole track (Fe-CI norm)	0.58 (0.01) 0.55 (0.01)	0.12 (0.01)	2.14 (0.01)	0.74 (0.01)	1.00	0.69 (0.01)	1.94 (0.01)	11.92 (0.02)	4.88 (0.15) 4.86 (0.14)	0.18 (0.04) 0.04 (0.002)	4.54 (0.04)	2.17 (0.40) 1.00 (0.08)	1.78 (0.66) 0.11 (0.01)	0.53 (0.18) 0.11 (0.01)	3.34 (1.04) 1.70 (0.31)	1.97 (0.38) 1.39 (0.18)

Notes for Tables 2a–g: Columns containing at least one upper limit value (italics) show two values for whole track masses and whole track Fe-CI-normalized abundances; the first assumes the upper limits are concentrations and the second assumes the upper limits are zero. The number in parentheses next to the "Whole track masses" label is the scaling factor (see text). Values in parentheses are random errors (1σ).

Table 2b.

	Element mass (femtograms)															
	S	Ca	Cr	Mn	Fe	Ni	Cu	Zn	Ga	Ge	Se	Br	Rb	Sr	Y	Zr
Track C2115,20																
20a	126 (3)	10.1 (0.3)	58.6 (2.6)	97.7 (1.1)	239 (1)	8.6 (0.2)	0.16 (0.10)	0.64 (0.10)	0.06 (0.06)	*0.08*	0.18 (0.06)	*0.02*	*0.02*	*0.02*	*0.01*	*0.01*
20b	nd	nd	4.3 (2.8)	1.28 (0.87)	66 (1)	11.5 (0.2)	0.09 (0.08)	0.09 (0.08)	*0.06*	*0.05*	*0.06*	*0.01*	*0.05*	0.04 (0.03)	*0.06*	0.49 (0.03)
20c	111 (5)	4.1 (0.4)	3.7 (0.7)	1.25 (0.30)	144 (1)	6.6 (0.1)	0.37 (0.05)	0.78 (0.05)	0.10 (0.03)	0.05 (0.03)	*0.06*	*0.03*	*0.08*	*0.01*	*0.05*	0.53 (0.02)
20d	nd	nd	4.1 (2.9)	1.74 (0.93)	94 (1)	4.2 (0.2)	0.47 (0.09)	0.51 (0.08)	0.09 (0.06)	0.07 (0.05)	0.09 (0.04)	0.05 (0.03)	0.04 (0.03)	0.04 (0.03)	0.10 (0.03)	0.37 (0.03)
20f	nd	nd	4.2 (2.7)	0.74 (0.84)	121 (1)	6.4 (0.2)	0.20 (0.08)	0.33 (0.08)	0.11 (0.06)	*0.04*	0.05 (0.03)	0.11 (0.03)	0.04 (0.03)	*0.01*	*0.03*	0.37 (0.03)
20j	nd	nd	8.7 (3.5)	2.89 (1.13)	171 (1)	9.8 (0.2)	0.26 (0.11)	0.57 (0.10)	*0.08*	0.14 (0.06)	0.11 (0.04)	0.06 (0.03)	0.06 (0.03)	0.04 (0.03)	0.09 (0.03)	0.23 (0.03)
20k	nd	nd	20.5 (1.5)	9.6 (0.5)	481 (1)	0.2 (0.1)	*0.10*	0.19 (0.04)	*0.07*	*0.05*	0.08 (0.02)	0.12 (0.02)	*0.04*	0.07 (0.01)	*0.04*	0.11 (0.01)
20l	nd	nd	3.8 (1.6)	1.11 (0.50)	51 (1)	1.5 (0.1)	0.29 (0.05)	0.42 (0.05)	0.13 (0.04)	*0.05*	*0.08*	*0.04*	*0.05*	*0.04*	*0.08*	0.25 (0.02)
20m	126 (5)	2.1 (0.4)	0.90 (0.10)	0.74 (0.10)	34 (0.2)	5.0 (0.1)	*1.02*	*1.29*	*0.55*	nd	nd	nd	nd	nd	nd	nd
20n	136 (5)	7.1 (0.5)	3.1 (0.2)	1.95 (0.10)	125 (0.5)	5.0 (0.1)	*1.32*	*1.58*	*0.43*	nd	nd	nd	nd	nd	nd	nd
20o	145 (5)	3.1 (0.5)	1.94 (0.10)	2.29 (0.10)	48 (0.3)	2.6 (0.1)	*1.31*	*1.35*	*0.40*	nd	nd	nd	nd	nd	nd	nd
20p	140 (5)	3.1 (0.4)	1.66 (0.10)	1.63 (0.10)	30 (0.2)	2.2 (0.1)	*1.22*	*1.12*	*0.52*	nd	nd	nd	nd	nd	nd	nd
20q	165 (6)	5.1 (0.4)	1.26 (0.10)	0.68 (0.10)	2 (0.1)	0.8 (0.1)	*1.45*	*1.36*	*0.46*	nd	nd	nd	nd	nd	nd	nd
Whole track masses (2.5)	6100 (70)	210 (4)	290 (18)	310 (4)	3970 (4)	160 (1)	20.4 (0.7) 4.6 (0.5)	25.3 (0.6) 8.7 (0.6)	7.5 (0.5) 1.2 (0.3)	1.51 (0.36) 0.75 (0.17)	2.06 (0.27) 1.45 (0.17)	1.30 (0.27) 1.00 (0.15)	1.11 (0.27) 0.43 (0.13)	0.77 (0.27) 0.53 (0.15)	1.34 (0.27) 0.55 (0.10)	6.85 (0.27) 6.81 (0.20)
Whole track (Fe-CI norm)	4.80 (0.06)	1.06 (0.02)	5.08 (0.31)	7.50 (0.11)	1.00	0.68(0.00)	9.51 (0.33) 2.12 (0.33)	3.81 (0.09) 1.31 (0.09)	35.9 (2.5) 5.69 (2.55)	2.14 (0.50) 1.06 (0.50)	4.79 (0.62) 3.37 (0.62)	16.8 (3.5) 13.0 (3.5)	23.4 (5.7) 9.0 (5.7)	4.5 (1.6) 3.1 (1.6)	44.6 (8.9) 18.3 (8.9)	84.1 (3.3) 83.6 (3.3)

Table 2c.

	Element mass (femtograms)															
	S	Ca	Cr	Mn	Fe	Ni	Cu	Zn	Ga	Ge	Se	Br	Rb	Sr	Y	Zr
Track C2115,21																
21a	nd	nd	28.7 (2.2)	23.5 (0.7)	1388 (2)	77.0 (0.2)	0.50 (0.06)	0.42 (0.05)	0.86 (0.04)	0.50 (0.03)	0.39 (0.02)	0.08 (0.02)	0.08 (0.02)	0.09 (0.02)	0.05 (0.02)	0.04 (0.02)
21b	nd	nd	20.9 (4.2)	24.5 (1.4)	2093 (4)	34.3 (0.3)	0.18 (0.10)	0.30 (0.10)	0.40 (0.07)	*0.10*	0.48 (0.04)	*0.01*	*0.05*	*0.06*	*0.03*	*0.07*
21c	nd	nd	12.6 (4.2)	12.7 (1.4)	1807 (4)	68.3 (0.4)	0.33 (0.11)	13.61 (0.15)	0.19 (0.08)	*0.10*	0.50 (0.05)	*0.01*	*0.02*	*0.03*	*0.02*	*0.04*
21d	nd	nd	15.3 (2.1)	8.9 (0.7)	972 (1)	11.0 (0.1)	0.25 (0.05)	0.29 (0.05)	0.25 (0.04)	*0.12*	0.30 (0.02)	*0.03*	*0.05*	*0.05*	*0.05*	*0.05*
21e	407 (8)	319 (2)	104 (2)	97.3 (0.8)	4027 (3)	175 (0.4)	3.02 (0.10)	2.38 (0.08)	1.79 (0.06)	*0.05*	0.58 (0.03)	*0.01*	0.10 (0.03)	0.11 (0.02)	*0.03*	0.05 (0.03)
21f	nd	nd	69.5 (3.2)	70.9 (1.1)	3042 (3)	83.6 (0.3)	0.81 (0.08)	0.69 (0.07)	1.01 (0.06)	0.11 (0.04)	0.59 (0.03)	0.06 (0.03)	0.13 (0.03)	0.10 (0.03)	*0.03*	0.04 (0.03)
21g	446 (9)	306 (2)	325 (4)	246.2 (1.5)	5609 (5)	180 (0.6)	3.55 (0.16)	2.81 (0.14)	3.14 (0.13)	*0.05*	0.66 (0.08)	0.09 (0.06)	0.15 (0.06)	0.06 (0.05)	*0.02*	*0.02*
21h	nd	nd	31.5 (2.1)	30.7 (0.7)	415 (1)	6.2 (1.0)	*0.05*	0.22 (0.05)	0.33 (0.04)	*0.02*	*0.03*	*0.01*	*0.01*	*0.01*	*0.01*	*0.01*
21i	nd	nd	*2.0*	*0.6*	214 (1)	0.7 (0.1)	0.16 (0.05)	3.18 (0.05)	*0.03*	*0.05*	*0.03*	*0.01*	*0.01*	*0.01*	*0.01*	*0.01*
21j	*148*	44 (0.5)	18.2 (0.2)	12.6 (0.1)	284 (1)	11.7 (0.1)	1.30 (0.04)	1.73 (0.04)	0.99 (0.05)	nd	nd	nd	nd	nd	nd	nd
21k	*107*	24 (0.7)	9.5 (0.2)	10.5 (0.2)	233 (1)	11.7 (0.1)	1.61 (0.06)	1.86 (0.06)	0.69 (0.05)	nd	nd	nd	nd	nd	nd	nd
21l	306 (7)	40 (0.8)	19.4 (0.3)	32.4 (0.6)	2442 (2)	131 (0.4)	2.63 (0.07)	18.12 (0.08)	0.88 (0.05)	nd	nd	nd	nd	nd	nd	nd
21m	270 (7)	126 (1.3)	50.7 (0.4)	45.6 (0.3)	1936 (2)	143 (0.4)	2.72 (0.09)	3.04 (0.09)	1.86 (0.05)	nd	nd	nd	nd	nd	nd	nd
21n	*146*	15 (0.7)	6.0 (0.2)	7.5 (0.2)	517 (1)	23.6 (0.2)	1.55 (0.07)	4.38 (0.09)	0.58 (0.05)	nd	nd	nd	nd	nd	nd	nd
21o	*101*	15 (0.8)	5.5 (0.2)	5.1 (0.2)	264 (1)	19.1 (0.2)	1.57 (0.08)	2.59 (0.09)	0.49 (0.05)	nd	nd	nd	nd	nd	nd	nd
21p	111 (5)	60 (0.9)	2.5 (0.1)	1.2 (0.1)	29 (0.3)	2.5 (0.1)	2.23 (0.08)	126 (0.4)	0.62 (0.05)	nd	nd	nd	nd	nd	nd	nd
21q	*101*	53 (0.8)	18.8 (0.1)	16.9 (0.2)	364 (1)	13.6 (0.1)	1.26 (0.06)	0.62 (0.05)	1.20 (0.05)	nd	nd	nd	nd	nd	nd	nd
Whole track masses (3.6)	12,700 (105) 10,200 (90)	5940 (12)	2690 (15) 2680 (15)	2350 (12) 2350 (7)	93,100 (30)	3610 (3)	86 (1)	660 (1)	55.6 (1) 55.5 (1)	5.23 (0.60) 2.91 (0.48)	16.89 (0.45) 16.63 (0.42)	1.41 (0.45) 1.09 (0.36)	2.74 (0.45) 2.17 (0.38)	2.49 (0.45) 1.73 (0.38)	1.15 (0.45) 0.23 (0.33)	1.50 (0.45) 0.61 (0.36)
Whole track (Fe-CI norm)	0.43 (0.004)	1.28 (0.003)	2.02 (0.01)	2.46 (0.01)	1.00	0.65 (0.001)	1.71 (0.02)	4.24 (0.01)	11.3 (0.2) 11.2 (0.1)	0.32 (0.04) 0.18 (0.03)	1.68 (0.04) 1.65 (0.04)	0.78 (0.25) 0.60 (0.20)	2.48 (0.41) 1.96 (0.34)	0.63 (0.11) 0.44 (0.09)	1.64 (0.64) 0.33 (0.46)	0.78 (0.23) 0.32 (0.19)

Table 2d.

	Element mass (femtograms)															
	S	Ca	Cr	Mn	Fe	Ni	Cu	Zn	Ga	Ge	Se	Br	Rb	Sr	Y	Zr
Track C2115,22																
22aa	251 (17)	4410 (9)	1150 (3)	805 (2)	32,700 (10)	77.1 (1)	1.24 (0.13)	22.0 (0.5)	56.5 (0.7)	*0.20*	0.14 (0.12)	*0.09*	0.95 (0.10)	0.50 (0.09)	0.58 (0.08)	0.45 (0.08)
22a	nd	nd	224 (176)	211 (43)	11,200 (69)	25.1 (1.8)	*0.60*	11.3 (0.61)	30.8 (0.7)	*0.19*	0.34 (0.11)	*0.08*	0.73 (0.08)	0.21 (0.08)	0.51 (0.07)	0.54 (0.07)
22b	nd	nd	135 (70)	70 (17)	4550 (20)	20.5 (0.7)	0.59 (0.25)	1.46 (0.18)	2.60 (0.13)	0.07 (0.07)	0.36 (0.05)	0.04 (0.04)	0.07 (0.03)	0.05 (0.03)	0.07 (0.03)	0.07 (0.03)
22c	nd	nd	265 (82)	281 (21)	14,300 (34)	22.0 (0.8)	*0.26*	2.73 (0.20)	2.97 (0.14)	*0.08*	1.93 (0.06)	*0.04*	0.11 (0.03)	0.06 (0.03)	0.11 (0.03)	0.11 (0.03)
22d	90 (8)	62.8 (1.2)	124 (40)	198 (10)	9220 (17)	12.9 (0.4)	0.91 (0.16)	3.38 (0.13)	2.72 (0.13)	*0.08*	0.56 (0.05)	0.06 (0.04)	0.09 (0.03)	0.04 (0.03)	0.07 (0.03)	0.09 (0.03)
22e	108 (8)	115 (2)	149 (40)	258 (10)	10,100 (26)	23.6 (0.7)	0.90 (0.26)	7.23 (0.25)	33.7 (0.5)	0.06 (0.14)	0.39 (0.09)	*0.07*	0.37 (0.06)	0.18 (0.06)	0.10 (0.06)	0.15 (0.06)
22f	nd	nd	124 (44)	70 (10)	3900 (12)	5.0 (0.4)	0.26 (0.16)	0.48 (0.10)	1.99 (0.08)	0.08 (0.05)	0.17 (0.03)	0.05 (0.02)	0.05 (0.02)	0.05 (0.02)	0.03 (0.02)	0.07 (0.02)
22g	nd	nd	120 (61)	112 (15)	7330 (21)	15.5 (0.6)	0.38 (0.20)	10.1 (0.2)	0.95 (0.10)	0.07 (0.06)	0.24 (0.04)	0.03 (0.03)	0.09 (0.02)	*0.03*	0.06 (0.02)	0.09 (0.02)
22h	nd	nd	121 (43)	28 (10)	2260 (9)	4.5 (0.4)	0.16 (0.16)	0.39 (0.10)	1.51 (0.08)	*0.05*	0.16 (0.03)	0.03 (0.02)	0.02 (0.02)	*0.02*	0.02 (0.02)	0.09 (0.02)
22i	nd	nd	233 (93)	126 (22)	6780 (31)	10.4 (0.8)	0.32 (0.32)	2.33 (0.24)	2.45 (0.17)	0.10 (0.09)	0.21 (0.06)	*0.04*	0.10 (0.04)	0.07 (0.04)	0.08 (0.04)	0.09 (0.04)
22j	nd	nd	133 (45)	42 (11)	5060 (14)	5.2 (0.4)	0.26 (0.15)	0.55 (0.10)	0.52 (0.07)	0.13 (0.05)	0.41 (0.03)	0.04 (0.02)	0.03 (0.02)	0.04 (0.02)	0.03 (0.02)	0.07 (0.02)
22k	nd	nd	80 (43)	35 (10)	3380 (11)	2.1 (0.3)	0.22 (0.16)	0.34 (0.10)	0.10 (0.07)	0.08 (0.05)	0.24 (0.03)	0.03 (0.02)	0.04 (0.02)	*0.02*	0.02 (0.02)	0.07 (0.02)
22l	nd	nd	148 (142)	70 (34)	5160 (43)	7.8 (1.3)	*0.49*	5.13 (0.43)	9.25 (0.37)	*0.14*	0.28 (0.09)	*0.07*	0.16 (0.06)	0.15 (0.07)	0.08 (0.06)	0.15 (0.06)
22m	nd	nd	100 (44)	22 (10)	2790 (10)	34.8 (0.5)	0.66 (0.16)	0.20 (0.10)	0.24 (0.07)	0.05 (0.05)	0.87 (0.03)	0.08 (0.02)	0.07 (0.02)	0.03 (0.02)	0.02 (0.02)	0.08 (0.02)
22n	nd	nd	74 (41)	14 (9)	609 (6)	39.4 (0.6)	1.05 (0.16)	0.35 (0.11)	0.11 (0.07)	0.62 (0.05)	0.27 (0.03)	0.03 (0.02)	0.05 (0.02)	0.02 (0.02)	0.02 (0.02)	0.10 (0.02)
22o	nd	nd	82 (42)	12 (9)	722 (6)	41.4 (0.6)	1.33 (0.16)	0.38 (0.10)	0.13 (0.07)	0.19 (0.05)	0.31 (0.03)	0.03 (0.02)	0.04 (0.02)	0.04 (0.02)	0.02 (0.02)	0.08 (0.02)
22p	nd	nd	71 (42)	18 (9)	1075 (7)	58.7 (0.6)	1.56 (0.17)	0.19 (0.10)	*0.07*	0.08 (0.05)	0.38 (0.03)	0.03 (0.02)	0.03 (0.02)	0.02 (0.02)	*0.02*	0.12 (0.02)
22r	nd	nd	54 (41)	10 (9)	6 (3)	0.8 (0.3)	0.37 (0.16)	91.4 (0.4)	0.20 (0.07)	*0.07*	0.06 (0.03)	2.26 (0.04)	0.25 (0.02)	0.02 (0.02)	*0.02*	0.13 (0.02)
22s	nd	nd	86 (41)	19 (9)	227 (4)	10.1 (0.4)	0.42 (0.16)	11.7 (0.2)	0.21 (0.07)	0.11 (0.05)	0.15 (0.03)	0.04 (0.02)	0.07 (0.02)	0.04 (0.02)	0.03 (0.02)	0.07 (0.02)
22t	nd	nd	218 (47)	126 (12)	7120 (16)	10.0 (0.4)	*0.16*	3.27 (0.13)	3.41 (0.09)	*0.05*	0.35 (0.03)	0.03 (0.02)	0.13 (0.02)	0.10 (0.02)	0.10 (0.02)	0.08 (0.02)
22u	nd	nd	54 (41)	20 (9)	536 (5)	2.7 (0.3)	0.21 (0.15)	0.16 (0.10)	1.77 (0.08)	*0.05*	0.03 (0.03)	0.02 (0.02)	0.03 (0.02)	0.02 (0.02)	*0.02*	0.02 (0.02)
22v	93 (5)	14.0 (0.6)	38 (0.2)	22 (0.3)	1480 (1)	2.2 (0.1)	0.66 (0.06)	0.71 (0.06)	0.59 (0.06)	0.06 (0.05)	0.03 (0.03)	*0.02*	0.03 (0.02)	*0.02*	0.02 (0.02)	0.02 (0.02)
22w	409 (11)	2810 (5)	1100 (1.8)	1380 (2)	47,700 (9)	143 (0.4)	2.17 (0.14)	38.9 (0.1)	92.2 (0.1)	nd	nd	nd	nd	nd	nd	nd
22x	189 (7)	35.7 (0.8)	18 (0.3)	16 (0.3)	1420 (2)	53.1 (0.3)	2.87 (0.08)	2.32 (0.07)	0.86 (0.06)	nd	nd	nd	nd	nd	nd	nd
Whole track masses (3.9)	7880 (190)	51,400 (30)	19,400 (770)	15,600 (190)	709,000 (190)	2480 (10)	71 (2.3) 65 (3.5)	860 (3)	971 (2) 970 (2)	15 (1.4) 9 (1.1)	43 (1.0)	17 (0.6) 15 (0.5)	19 (0.6)	9 (0.6) 9 (0.5)	11 (0.6) 11 (0.5)	15 (0.6)
Whole track (Fe-CI norm)	0.04 (0.001)	1.46 (0.001)	1.91 (0.08)	2.15 (0.03)	1.00	0.06 (0.001)	0.19 (0.01) 0.17 (0.01)	0.72(0.002)	25.83 (0.05) 25.82 (0.05)	0.12 (0.01) 0.07 (0.01)	0.56(0.01)	1.26 (0.04) 1.10 (0.04)	2.26 (0.07)	0.31 (0.02) 0.29 (0.02)	2.04 (0.11) 1.98 (0.10)	1.03 (0.04)

Table 2e.

	Element mass (femtograms)							
	S	Ca	Cr	Mn	Fe	Ni	Cu	Zn
Track C2044,12								
12a	424 (6)	6.5	519 (1.8)	91 (0.4)	41,700 (420)	3850 (0.3)	19.03	0.65
12b	61 (4)	6.5	19 (0.6)	1.7	1130 (52)	132 (0.6)	5.23 (0.18)	0.65
12c	17	6.5	10 (0.5)	1.7	557 (1)	65 (1.6)	4.21 (0.16)	1.89 (0.12)
12d	17	6.5	12 (0.5)	1.7	626 (1)	82 (0.5)	4.07 (0.17)	2.15 (0.12)
12e	17	6.5	6 (0.4)	1.7	386 (1)	47 (0.4)	3.29 (0.15)	2.25 (0.11)
12f	39	6.5	10 (0.4)	1.7	393 (3)	49 (0.4)	3.62 (0.15)	1.79
12g	45 (3)	6.5	2.0	1.7	99 (1)	11 (0.2)	2.36	1.55
12h	22	6.5	6.6	1.7	213 (1)	25 (0.3)	2.72	0.65
12i	35 (2)	6.5	6 (0.3)	1.7	284 (1)	33 (0.3)	2.15	0.65
12j	31	6.5	17 (0.5)	1.7	826 (2)	115 (0.6)	4.15 (0.16)	1.90 (0.11)
12k	46 (3)	6.5	19 (0.5)	1.7	1030 (5)	127 (1.8)	3.40 (0.15)	1.69 (0.10)
12l	17	6.5	12 (0.5)	1.7	754 (2)	92 (0.5)	3.22	1.38
12m	47	6.5	14 (0.4)	1.7	638 (1)	81 (1.5)	3.21 (0.13)	1.34
12n	17	6.5	14 (0.4)	1.7	821 (2)	101 (1.6)	2.67	1.28
12o	17	6.5	12 (0.4)	1.7	659 (1)	80 (0.5)	2.37 (0.11)	1.38 (0.11)
12p	17	6.5	10 (0.4)	1.7	609 (1)	79 (1.3)	2.36	1.11
12q	17	6.5	23 (0.2)	1.7	353 (1)	30 (1.4)	0.72	0.65
12r	17	6.5	16 (1.6)	1.7	344 (1)	41 (1.7)	0.70	0.65
Whole track masses (7)	6320 (120) 4270 (60)	820 (0)	5090 (10) 5030 (10)	840 (10) 640 (3)	360,000 (3500)	35,300 (30)	490 (4) 230 (3)	170 (3) 80 (2)
Whole track (Fe-CI norm)	0.06 (0.001) 0.04 (0.001)	0.05 0.00	0.99 (0.01) 0.98 (0.002)	0.23 (0.004) 0.17 (0.001)	1.00	1.65 (0.02)	2.50 (0.03) 1.21(0.02)	0.27 (0.01) 0.13(0.003)

Table 2f.

	Element mass (femtograms)								
	S	Ca	Cr	Mn	Fe	Ni	Cu	Zn	Ga
Track C2044,7									
7a	*98*	66 (1)	36.3 (0.7)	10.8 (0.6)	2860 (9)	193 (0.8)	5.93 (0.18)	6.26 (0.17)	1.83 (0.37)
7b	122 (5)	71 (1)	31.3 (0.7)	12.6 (0.6)	3030 (9)	205 (0.8)	7.82 (0.23)	10.1 (0.2)	*0.30*
7c	179 (7)	151 (3)	78.2 (0.8)	71.9 (0.9)	2770 (8)	180 (0.8)	6.59 (0.20)	12.5 (0.2)	*0.30*
7d	254 (10)	360 (7)	85.2 (1.3)	57.8 (1.1)	9820 (16)	628 (1.4)	15.8 (0.5)	10.6 (0.4)	1.11 (0.22)
7e	261 (11)	146 (3)	65.5 (1.0)	24.8 (0.8)	6330 (12)	432 (1.2)	10.7 (0.3)	9.14 (0.27)	*0.30*
7f	179 (7)	68 (1)	26.8 (0.6)	11.4 (0.6)	2560 (8)	164 (0.7)	5.77 (0.17)	11.2 (0.2)	*0.30*
Whole track masses (9)	9840 (180) 8960 (160)	7750 (70)	2910 (20)	1700 (20)	246,000 (200)	16,200 (20)	470 (7)	540 (6)	40 (7) 30 (4)
Whole track (Fe-CI norm)	0.13 (0.002) 0.11 (0.002)	0.63 (0.01)	0.83 (0.01)	0.67 (0.01)	1.00	1.11 (0.002)	3.56 (0.05)	1.30 (0.01)	2.86 (0.51) 2.03 (0.29)

Table 2g.

	Element mass (femtograms)								
	S	Ca	Cr	Mn	Fe	Ni	Cu	Zn	Ga
Track C2027,48									
48-1a	89 (6)	2190 (7)	5.8 (0.7)	*1.8*	31 (0.4)	44.2 (0.4)	15.5 (0.3)	282 (1)	*0.6*
48-1b	*17*	872 (4)	*4.0*	*1.8*	11 (0.4)	1.5 (0.3)	11.6 (0.3)	3.8 (0.2)	*0.6*
48-1c	*17*	258 (3)	*5.1*	*1.8*	38 (0.5)	10.6 (0.3)	12.6 (0.3)	77.3 (0.4)	*0.6*
48-1d	*17*	1450 (7)	6.1 (0.7)	*1.8*	76 (0.6)	7.3 (0.4)	16.3 (0.4)	2440 (2)	*0.6*
48-1e	282 (7)	901 (5)	6.8 (0.7)	*3.3*	108 (0.7)	11.3 (0.3)	15.8 (0.4)	1130 (2)	*0.6*
48-1f	*56*	27 (2)	16.5 (0.7)	12.0 (0.6)	714 (1)	66.2 (0.5)	12.6 (0.3)	*1.5*	*0.6*
48-1g	*57*	52 (1)	26.4 (0.8)	17.2 (0.7)	1250 (3)	93.1 (0.6)	11.6 (0.3)	1.4 (0.2)	*0.6*
48-1h	*17*	*15*	10.7 (0.8)	27.4 (0.6)	1250 (3)	3.9 (0.3)	10.4 (0.3)	2.9 (0.2)	*0.6*
48-1i	883 (9)	37 (3)	47.2 (0.9)	53.6 (0.9)	13,900 (7)	178 (1)	11.5 (0.3)	3.2 (0.2)	*0.6*
48-1j	*104*	196 (3)	228 (2)	440 (2)	17,400 (7)	99.7 (0.6)	12.4 (0.3)	4.1 (0.2)	3.5 (0.2)
48-1k	87 (6)	157 (3)	79.5 (0.8)	66.7 (0.9)	4320 (3)	280 (1)	13.3 (0.3)	3.2 (0.2)	*0.6*
48-1l	160 (7)	312 (3)	169.38 (1)	148 (1)	8790 (5)	566 (1)	16.6 (0.3)	2.0 (0.2)	*0.6*
48-1m	125 (7)	215 (3)	112 (1)	89.3 (0.9)	5540 (4)	332 (0.2)	16.4 (0.3)	11.5 (0.2)	*0.6*
48-1n	126 (7)	280 (5)	161 (2)	168 (1)	8710 (5)	484 (1)	18.0 (0.3)	12.0 (0.2)	*1.0*
48-1o	*63*	177 (2)	107 (1)	142 (1)	6960 (5)	306 (1)	14.9 (0.3)	12.1 (0.2)	*1.3*
48-1p	143 (6)	279 (4)	94.7 (1.1)	73.8 (0.9)	4770 (4)	325 (1)	15.7 (0.3)	27.7 (0.3)	*0.9*
48-1q	107 (5)	166 (2)	78.7 (1.0)	59.3 (0.8)	3960 (4)	318 (1)	15.0 (0.3)	8.0 (0.2)	*0.6*
48-1r	*71*	72 (1)	25.5 (0.7)	19.0 (0.6)	1210 (2)	88.4 (0.5)	11.0 (0.3)	7.8 (0.2)	*0.6*
48-1s	113 (6)	97 (1)	50.7 (0.9)	34.9 (0.7)	2530 (3)	187 (1)	13.5 (0.3)	12.1 (0.2)	*0.6*
48-1t	160 (6)	133 (2)	58.1 (1.0)	48.6 (0.8)	3980 (4)	302 (1)	14.1 (0.3)	5.2 (0.2)	*0.6*
48-1u	263 (7)	*8*	*7.6*	*1.8*	3090 (3)	27.5 (0.4)	10.1 (0.3)	3.2 (0.2)	*0.6*
48-1v	145 (7)	166 (4)	242 (2)	211 (1)	3630 (3)	174 (1)	13.2 (0.3)	11.7 (0.2)	*0.6*
48-1w	213 (7)	101 (2)	48.5 (1.0)	35.1 (0.7)	3540 (3)	198 (1)	13.1 (0.3)	8.7 (0.2)	*0.6*
48-1x	169 (6)	237 (3)	161 (1)	87.3 (0.9)	5200 (4)	361 (1)	14.6 (0.3)	6.6 (0.2)	*0.6*
48-1y	166 (7)	324 (3)	151 (1)	119 (1)	7380 (4)	479 (0.3)	18.0 (0.3)	4.1 (0.2)	*0.6*
48-1z	*69*	94 (2)	62.7 (0.9)	38.7 (0.7)	2350 (3)	188 (1)	11.2 (0.3)	4.2 (0.2)	*0.6*
48-1aa	139 (6)	123 (2)	53.0 (0.9)	38.8 (0.7)	2580 (4)	206 (1)	11.5 (0.3)	3.2 (0.2)	*0.6*
48-1ab	149 (4)	170 (2)	146 (1)	69.1 (0.9)	5840 (4)	408 (1)	12.6 (0.3)	1.5 (0.2)	*0.6*
48-1ac	*17*	154 (2)	145 (1)	93.9 (0.9)	6280 (4)	442 (1)	14.5 (0.3)	3.1 (0.2)	2.5 (0.2)
48-1ad	*61*	168 (3)	114 (1)	102 (1)	4790 (4)	451 (1)	13.3 (0.3)	2.4 (0.2)	*0.6*
48-1ae	*17*	47 (1)	43.8 (0.9)	27.3 (0.6)	1810 (2)	145 (1)	12.3 (0.3)	6.5 (0.2)	*0.9*
48-1af	*52*	94 (4)	54.7 (0.9)	41.7 (0.7)	2530 (3)	164 (1)	11.6 (0.3)	5.0 (0.2)	*0.6*
48-2a	*71*	1290 (6)	949 (3)	976 (2)	39,800 (10)	437 (1)	14.5 (0.4)	9.0 (0.2)	7.8 (0.2)
48-2b	*17*	620 (5)	2690 (4)	1730 (3)	68,200 (10)	284 (1)	7.1 (0.3)	6.4 (0.2)	12.3 (0.2)
48-2c	*17*	206 (4)	832 (3)	1480 (3)	61,400 (10)	139 (0.1)	*2.9*	5.4 (0.2)	*0.6*
48-2d	99 (6)	*8*	*20.1*	48.1 (0.1)	11,800 (6)	207 (1)	5.9 (0.2)	120 (1)	*0.6*
48-2e	*17*	29 (1)	35.5 (0.7)	14.2 (0.5)	1190 (2)	75 (1)	2.5 (0.2)	11.8 (0.2)	*0.6*
48-3a	136 (5)	91 (2)	41.4 (0.8)	37.7 (0.6)	2930 (3)	236 (1)	4.1 (0.2)	13.3 (0.2)	*0.6*
48-3b	76 (3)	65 (2)	20.6 (0.6)	16.1 (0.5)	1330 (2)	99 (1)	2.1 (0.1)	11.3 (0.2)	*0.6*
48-3c	66 (3)	63 (2)	35.8 (0.6)	24.1 (0.5)	1420 (2)	127 (1)	1.8 (0.1)	11.1 (0.2)	*0.6*
48-3d	85 (4)	73 (2)	26.2 (0.6)	55.6 (0.7)	1930 (2)	398 (1)	4.2 (0.1)	9.6 (0.2)	*0.6*

Table 2g. *Continued.*

	Element mass (femtograms)								
	S	Ca	Cr	Mn	Fe	Ni	Cu	Zn	Ga
48-3e	41	36 (1)	11.3 (0.5)	16.8 (0.4)	980 (2)	69 (0.4)	1.3 (0.1)	7.5 (0.1)	0.6
48-3f	117 (4)	88 (2)	49.4 (0.7)	34.7 (0.6)	2590 (3)	157 (1)	2.8 (0.1)	6.0 (0.1)	*0.6*
48-3g	*48*	43 (1)	67.0 (0.7)	14.5 (0.5)	1590 (7)	134 (1)	3.1 (0.1)	6.1 (0.1)	*0.6*
48-3h	*36*	43 (2)	38.2 (0.8)	132 (1)	5560 (4)	36 (0.4)	1.2 (0.1)	7.6 (0.1)	*0.6*
48-3i	171 (6)	341 (3)	202 (1)	256 (1)	8270 (5)	589 (1)	11.8 (0.2)	10.8 (0.2)	*0.6*
48-3j	*81*	44 (1)	31.8 (0.6)	16.7 (0.5)	1480 (2)	81 (1)	2.4 (0.1)	9.5 (0.2)	*0.6*
48-3k	43 (3)	90 (2)	42.2 (0.7)	25.9 (0.5)	1840 (2)	117 (1)	4.9 (0.2)	11.2 (0.2)	*0.6*
48-3l	*17*	92 (2)	46.6 (0.8)	37.1 (0.5)	2450 (3)	177 (1)	3.3 (0.2)	11.3 (0.2)	*0.6*
48-3m	159 (4)	178 (2)	83.0 (0.9)	57.6 (0.8)	3610 (3)	232 (1)	4.4 (0.2)	7.3 (0.1)	*0.6*
48-3n	*17*	34 (1)	26.8 (0.6)	14.1 (0.4)	920 (2)	47 (0.4)	*0.8*	9.0 (0.1)	*0.6*
48-3o	199 (5)	230 (3)	108 (1)	79.5 (0.8)	5000 (4)	382 (1)	7.4 (0.2)	9.4 (0.2)	*0.6*
48-3p	167 (5)	127 (2)	48.6 (0.8)	40.6 (0.7)	2770 (3)	179 (1)	4.0 (0.2)	15.8 (0.2)	*0.6*
48-3q	*78*	70 (2)	28.2 (0.7)	22.4 (0.5)	1320 (2)	92 (1)	*2.3*	13.6 (0.2)	*0.6*
48-3r	*17*	41 (1)	57.1 (0.7)	47.2 (0.6)	1540 (2)	85 (1)	*1.8*	10.3 (0.2)	*0.6*
Whole track masses	35,600 (270)	81,000 (90)	48,100 (40)	44,700 (40)	2,187,000 (100)	68,000 (40)	3190 (10)	26,600 (10)	350 (9)
(6)	28,800 (190)	80,700 (90)	47,900 (40)	44,300 (40)			3140 (10)	26,600 (10)	160 (2)
Whole track	0.05 (0.001)	0.74 (0.001)	1.54 (0.001)	1.99 (0.002)	1.00	0.52 (0.001)	2.70 (0.01)	7.27 (0.002)	3.03 (0.08)
(Fe-CI norm)	0.04 (0.001)	0.74 (0.001)	1.53 (0.001)	1.97 (0.002)			2.66 (0.01)	7.27 (0.002)	1.35 (0.02)

Zn. The terminal particle for C2115,20 is closer to chondritic than the whole track. C2115,21 again shows a large fractionation in Zn with the whole track enriched and the terminal particle depleted. The patterns for C2115,22 are similar, with the exceptions of Se and Br, which are fractionated by an order of magnitude. This similarity is largely due to the fact that the terminal particle represents a major fraction of the whole track mass (70% Fe). The C2044,12 terminal particle is depleted in Zn (and Cu to a lesser extent) relative to the whole track. The C2044,7 terminal particle is fairly representative of the whole track with the exceptions of Ga and possibly S. The C2027,48 terminal particle is depleted in S, Cu, and Zn relative to the whole track.

The generally high Ga concentrations in these samples are remarkable. Such enrichments have not been seen in IDPs, for example. Geochemically, Ga^{3+} often follows Al^{3+}. Both are strongly hydrolyzing group III elements, and gallium is a common trace element in aluminous minerals such as corundum, diaspore, boehmite, gibbsite, and a variety of clay minerals (Hill et al. 1952). Ga^{3+} can also show an affinity with Fe^{3+} and can be enriched in magnetite and maghemite (Lawrenchuck and Seruck 1966). It is unclear at this point what specific mineral phase these high Ga abundances are associated with, but they may reflect an association with an aluminum-rich refractory phase. What is clear is that virtually all the fragments analyzed are enriched in Ga relative to CI.

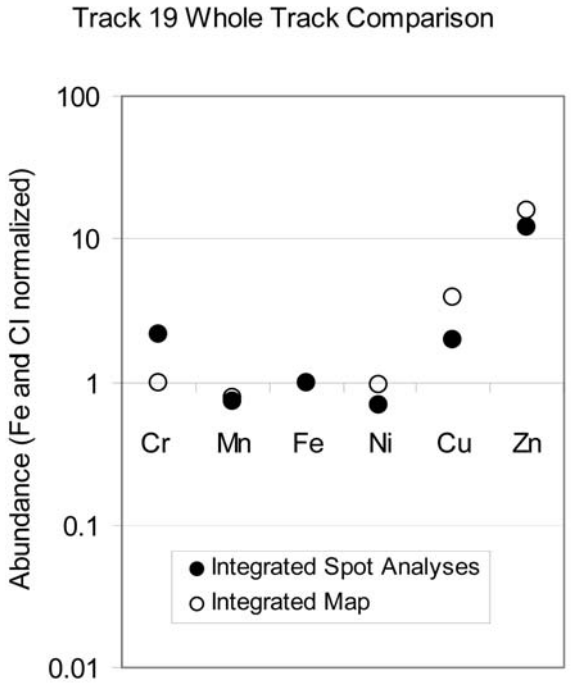

Fig. 3. Comparison of the Fe- and CI-normalized elemental whole-track composition of C2115,19 measured using the SXRF microprobe at APS using the integrated-particle technique and the mapping technique. There is good agreement between the measurements by the two techniques (after Flynn et al. 2006, supplemental information).

Individual Fragment Compositions and Impactor Heterogeneity

The Stardust impactors have been disaggregated during capture; cometary fragments along a track's walls represent up to an order of magnitude larger mass than that preserved in the terminal particle (Zolensky et al. 2006; Flynn et al.2006; Hörz et al. 2006). The data presented here offer an opportunity to evaluate the heterogeneity of these impactor particles, study element correlations in the fragments, and search for correlations between element abundances and other properties of the tracks, such as morphology and length.

Tables 2a–g show the elemental masses (S through Zr) for the 156 individual fragments analyzed in this work. Tables 3a–g show the corresponding Fe and CI normalized abundances for each fragment. As can be seen, the fragments have diverse compositions. As an example, Fig. 5 shows the abundance patterns for 20 fragments analyzed in C2115,19 (after Fig. 1 of Flynn et al. 2006). As mentioned above, the abundance pattern for the sum of the fragments is near CI with depletions in Ca and Ge and enrichments in the moderately volatile elements Zn, Ga, and Se. The variation among fragments is up to three orders of magnitude.

The large number of fragments analyzed along the lengths of the tracks offers the opportunity to evaluate compositional variations with distance from the entry point. Such variations might be produced, for example, if volatile elements were preferentially being lost early in the capture process. In general, the observed "along-track" trends in element abundances are subtle. The most pronounced effects were seen in C2115,19 (Fig. 6), where Zn exhibits a decrease with distance from the entry point, while Cr is most abundant near the end of the track. Sulfur is reasonably uniform. Similar plots for C2115,21 and C2115,22 show no obvious systematic trends with distance. These observations support the interpretation that material is lost from the impactor during capture primarily by disaggregation rather than volatilization. However, volatilization can be significant in some cases, as evidenced by the C2115,19 Zn distribution.

Figures 7a–h show plots of elemental mass (Ni, Ca, Cr, Mn, Cu, Ga, Zn, and S) versus the elemental mass of Fe for each of the 156 fragments analyzed with specific symbols for each track. The figures are presented roughly in order of increasing volatility; open squares represent individual fragment analyses and solid squares are the sums of all fragments within a given track. The dashed lines represent the ratio of the two respective elements in CI meteorites (CI). Differences in fragment mass are discernible on these plots with low-mass fragments occurring at the lower left and high-mass fragments occurring at the upper right. On the Ni versus Fe plot, the majority of the fragments fall along the CI line, indicating a good correlation between these elements. However, it can be seen that the C2115,22

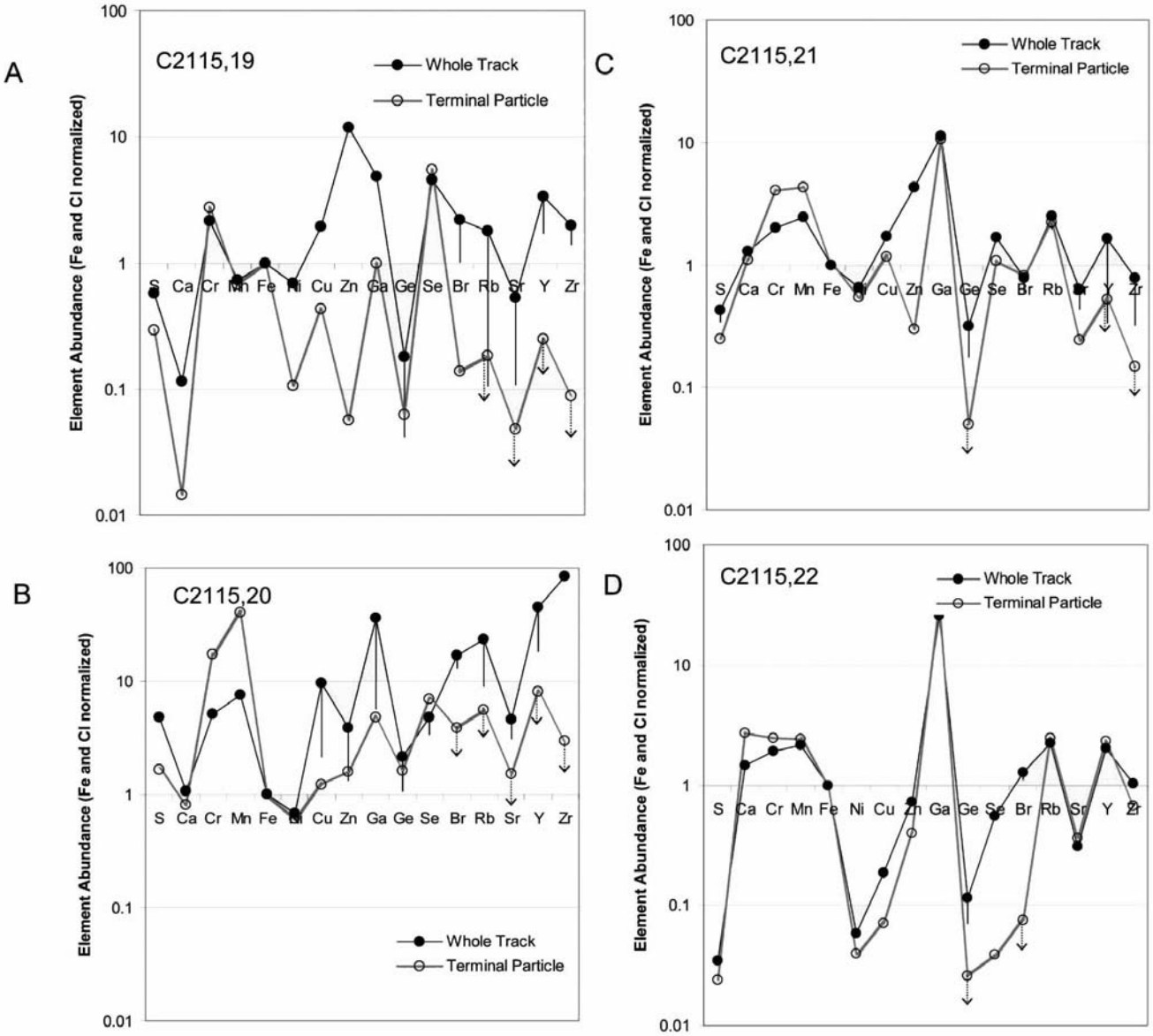

Fig. 4. a–d) Elemental abundance patterns for whole tracks and terminal particles for the seven tracks in this study. The whole-track patterns were produced by summing the element masses for all particles analyzed for a given track, multiplying by the ratio of total Fe in the map and total Fe in the particles, and normalizing by Fe and the CI abundance. A flat profile at unity represents the CI abundances. The patterns are generally near CI abundance but show diverse features in detail, including S and Ca depletions and Cu, Zn, and Ga enrichments. Vertical lines on the whole track patterns represent the range of possible values for elements for which the masses of one or more fragments were upper limits. Downward pointing arrows for the terminal particle patterns indicate upper limits.

fragments lie predominately on a parallel trend roughly a factor of 10 lower in Ni, which is consistent with the whole-track abundance pattern (Fig. 4d). The Ca plot shows the observed depletion for C2115,19 and that these are largely low-mass fragments. We can also see that although most of the C2027,48 fragments fall on the CI trend, some are Ca-enriched. These may be interesting high-Ca indigenous phases, or they could be aerogel contamination (Ca-rich particles known to be aerogel contaminants), but are obviously worth investigating further. Chromium and Mn show similar distributions to Ca but without the highly enriched fragments. Copper shows a randomly dispersed distribution about the CI ratio. The ubiquitous enrichment in Ga is easily discerned on the Ga plot, particularly represented by the C2115,22 fragments. The Zn plot shows several interesting features. There tends to be a generally tight clustering within a given track. The principal exception is C2027,48, which displays a trend moving from the CI trend to high Zn values. Several of the other tracks have a high

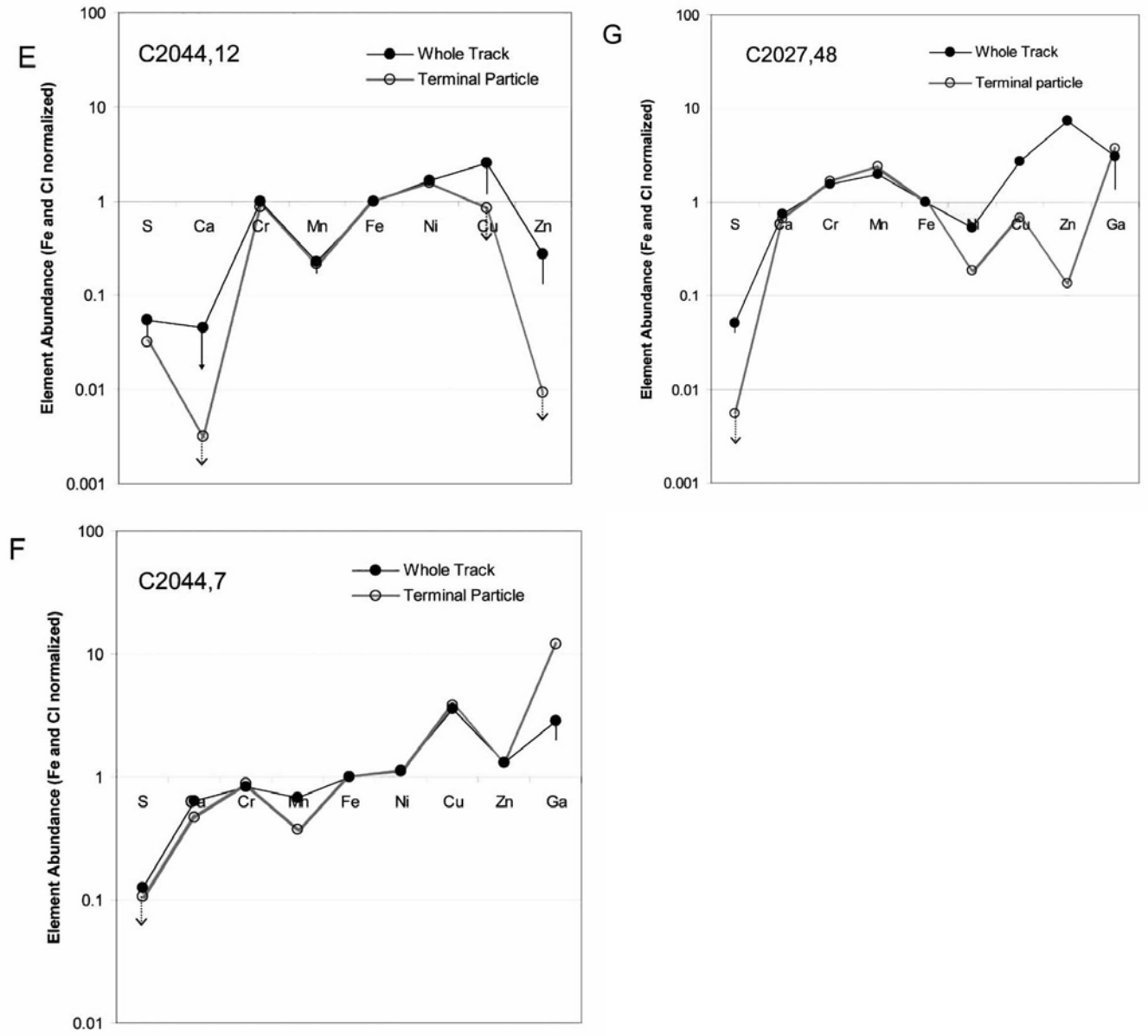

Fig. 4. *Continued*. e–g) Elemental abundance patterns for whole tracks and terminal particles for the seven tracks in this study. The whole-track patterns were produced by summing the element masses for all particles analyzed for a given track, multiplying by the ratio of total Fe in the map and total Fe in the particles, and normalizing by Fe and the CI abundance. A flat profile at unity represents the CI abundances. The patterns are generally near CI abundance but show diverse features in detail, including S and Ca depletions and Cu, Zn, and Ga enrichments. Vertical lines on the whole track patterns represent the range of possible values for elements for which the masses of one or more fragments were upper limits. Downward pointing arrows for the terminal particle patterns indicate upper limits.

Zn fragment of this kind. The principal Zn depletions are shown by the highly fractionated track C2115,22. The ubiquitous S depletion can been seen in the S plot with the principal exception being C2115,19 whose fragments fall on the CI trend.

Of the elements analyzed, Fe is likely to be the least volatile and typically present in highest concentration. The Ni/Fe ratio should be least modified by capture-heating effects. From these plots, it is apparent that although significant variations exist in the elemental masses of individual fragments within each track, masses and elemental ratios do cluster for given tracks when they are compared to each other. For most of the fragment populations Ni/Fe, Ca/Fe, Cr/Fe, and Mn/Fe are similar to the ratios found in CI meteorites. Many of the track C2115,19 fragments have Ca/Fe, Cr/Fe, and Mn/Fe ratios lower than CI, but from Fig. 7 it is apparent that this represents some of the lowest mass fragments analyzed and may reflect increased error in accurately determining the Ca, Cr, and Mn mass. Many of the fragments from track

Table 3a.

	Elemental abundances (Fe- and CI-normalized)															
	S	Ca	Cr	Mn	Fe	Ni	Cu	Zn	Ga	Ge	Se	Br	Rb	Sr	Y	Zr
Track C2115,19																
19a	0.29 (0.002)	0.01 (0.001)	2.71 (0.00)	0.68 (0.001)	1.00	0.11 (0.001)	0.43 (0.02)	0.06 (0.01)	0.99 (0.25)	0.06 (0.04)	5.47 (0.11)	*0.34*	*0.2*	*0.0*	*0.2*	*0.1*
19b	1.09 (0.07)	0.15 (0.03)	1.72 (0.03)	0.56 (0.03)	1.00	1.28 (0.004)	2.56 (0.24)	12.5 (0.09)	4.32 (1.25)	*0.2*	2.55 (0.73)	*5.6*	*2.6*	*0.7*	*4.1*	*1.5*
19c	0.68 (0.06)	0.07 (0.03)	0.10 (0.03)	0.14 (0.03)	1.00	1.67 (0.005)	2.09 (0.21)	6.88 (0.09)	2.89 (1.36)	*0.2*	1.64 (0.53)	19.7 (2.97)	*2.9*	*0.8*	*4.5*	4.79 (2.82)
19d	1.38 (0.03)	0.77 (0.02)	1.01 (0.04)	0.73 (0.05)	1.00	1.06 (0.01)	4.46 (0.31)	5.28 (0.10)	18.8 (2.0)	*0.4*	1.87 (1.17)	4.48 (4.32)	*4.2*	*1.2*	*6.4*	*2.4*
19e	0.96 (0.12)	0.08 (0.06)	0.06 (0.04)	*0.05*	1.00	1.94 (0.01)	1.80 (0.43)	1.24 (0.11)	2.56 (2.21)	*0.4*	2.75 (0.87)	8.05 (4.81)	*4.6*	*1.3*	*7.2*	*6.2*
19f	0.71 (0.11)	0.06 (0.05)	0.13 (0.04)	0.06 (0.05)	1.00	0.62 (0.01)	0.98 (0.33)	5.16 (0.11)	2.10 (2.09)	*0.4*	2.39 (0.82)	*2.7*	*4.4*	*1.2*	*6.8*	*2.6*
19g	0.86 (0.10)	0.50 (0.05)	1.02 (0.04)	0.64 (0.05)	1.00	0.96 (0.01)	1.40 (0.61)	3.74 (0.15)	4.72 (3.87)	*0.7*	2.87 (0.76)	*5.0*	*8.1*	*2.3*	*12.5*	*4.7*
19h	1.04 (0.04)	0.50 (0.02)	10.2 (0.04)	5.30 (0.03)	1.00	0.40 (0.005)	1.53 (0.10)	0.47 (0.05)	2.61 (1.28)	*0.2*	2.13 (0.25)	*1.7*	*2.7*	*0.8*	*4.2*	*1.6*
19i	0.62 (0.19)	*0.09*	0.09 (0.07)	0.12 (0.07)	1.00	0.45 (0.01)	0.77 (0.28)	6.30 (0.14)	4.83 (3.57)	*0.6*	3.10 (1.40)	*4.7*	*7.5*	*2.1*	*11.6*	*4.4*
19j	0.73 (0.03)	0.10 (0.02)	0.11 (0.01)	0.14 (0.02)	1.00	0.42 (0.004)	0.87 (0.10)	3.72 (0.05)	2.92 (1.24)	*0.2*	2.54 (0.24)	*1.6*	*2.6*	*0.7*	*4.1*	*1.5*
19k	0.86 (0.07)	0.06 (0.03)	0.21 (0.03)	0.19 (0.03)	1.00	0.85 (0.01)	1.68 (0.12)	11.5 (0.06)	2.93 (1.57)	*0.3*	2.60 (0.62)	*2.1*	*3.3*	*0.9*	*5.1*	*1.9*
19l	0.82 (0.04)	0.09 (0.02)	0.08 (0.02)	0.02 (0.02)	1.00	0.89 (0.01)	0.96 (0.12)	1.38 (0.06)	*1.02*	*0.3*	2.76 (0.31)	*2.0*	*3.3*	*0.9*	*5.1*	3.95 (1.61)
19m	1.01 (0.15)	0.08 (0.07)	0.75 (0.06)	0.35 (0.06)	1.00	0.82 (0.02)	1.25 (0.46)	6.96 (0.22)	4.52 (5.81)	*1.0*	2.14 (1.14)	*7.6*	*12.1*	*3.4*	31.5 (16.3)	11.1 (6.0)
19n	0.89 (0.05)	0.15 (0.03)	0.20 (0.02)	0.10 (0.02)	1.00	1.38 (0.01)	2.75 (0.16)	4.77 (0.08)	2.07 (2.00)	*0.4*	2.83 (0.39)	*2.6*	*4.2*	*1.2*	9.9 (5.6)	3.53 (2.06)
19p	1.41 (0.14)	0.26 (0.07)	0.15 (0.05)	1.81 (0.06)	1.00	1.63 (0.02)	6.04 (0.41)	108. (0.2)	7.22 (5.22)	*0.9*	4.97 (1.02)	20.9 (5.7)	*10.9*	4.55 (2.59)	24.0 (14.6)	25.2 (5.4)
19q	1.10 (0.15)	0.23 (0.07)	0.14 (0.06)	1.74 (0.07)	1.00	5.92 (0.02)	7.65 (0.45)	104 (0.2)	10.0 (5.8)	*1.0*	5.24 (1.13)	*7.5*	*12.1*	5.51 (2.87)	28.0 (16.2)	15.3 (6.0)
19r	1.17 (0.27)	0.22 (0.13)	0.19 (0.11)	0.64 (0.11)	1.00	9.11 (0.04)	7.91 (0.81)	88 (0.4)	10.0 (10.3)	*1.8*	5.47 (2.03)	*13.5*	*21.6*	*6.0*	49.6 (29.0)	34.7 (10.7)
19s	1.06 (0.07)	0.26 (0.04)	0.28 (0.03)	0.29 (0.03)	1.00	3.26 (0.01)	6.24 (0.22)	2.20 (0.11)	5.13 (2.79)	*0.5*	1.92 (0.55)	*3.6*	7.16 (4.97)	2.19 (1.38)	13.7 (7.8)	17.8 (2.9)
19t	1.24 (0.09)	0.18 (0.04)	0.07 (0.03)	1.22 (0.04)	1.00	7.84 (0.01)	5.41 (0.25)	47.5 (0.1)	4.73 (3.21)	*0.6*	5.60 (0.63)	*4.2*	*6.7*	*1.9*	19.1 (9.0)	11.9 (3.3)
19u	0.89 (0.15)	0.30 (0.07)	0.28 (0.06)	2.18 (0.07)	1.00	3.52 (0.02)	7.57 (0.46)	129 (0.2)	8.16 (5.83)	*1.0*	6.17 (1.14)	*7.6*	*12.2*	*3.4*	34.3 (16.3)	18.7 (6.0)
19v	*31*	19.8 (0.9)	3.88 (1.31)	8.24 (0.91)	1.00	1.68 (0.31)	279 (10)	7608 (6)	1399 (88)	nd	nd	nd	nd	nd	nd	nd
19w	1.05 (0.05)	0.38 (0.02)	0.59 (0.04)	0.52 (0.03)	1.00	3.02 (0.02)	14.3 (0.3)	4.68 (0.11)	27.2 (2.8)	nd	nd	nd	nd	nd	nd	nd
19x	1.21 (0.04)	0.37 (0.03)	0.56 (0.04)	0.55 (0.03)	1.00	0.74 (0.01)	6.80 (0.30)	9.30 (0.08)	27.5 (2.5)	nd	nd	nd	nd	nd	nd	nd

Notes for Tables 3a–g: Values in italics are upper limits. Values in parentheses are random uncertainties (1σ).

Table 3b.

	Elemental abundances (Fe- and CI-normalized)															
	S	Ca	Cr	Mn	Fe	Ni	Cu	Zn	Ga	Ge	Se	Br	Rb	Sr	Y	Zr
Track C2115,20																
20a	1.65 (0.04)	0.81 (0.03)	17.1 (0.8)	39.8 (0.45)	1.00	0.61 (0.01)	1.21 (0.70)	1.59 (0.25)	4.77 (4.74)	*1.9*	6.95 (2.32)	*3.8*	*5.6*	*1.5*	*8.1*	*3.0*
20b	nd	nd	4.56 (2.97)	1.89 (1.33)	1.00	2.93 (0.05)	2.59 (2.53)	0.86 (0.72)	*17*	*4.1*	*9.0*	*6.9*	*61*	13.3 (10.7)	*128*	362 (22)
20c	2.43 (0.11)	0.61 (0.06)	1.79 (0.34)	0.84 (0.20)	1.00	0.77 (0.01)	4.79 (0.64)	3.24 (0.21)	13.3 (3.9)	2.09 (1.17)	*4.1*	*12.0*	*46.1*	*2.3*	*42*	179 (7)
20d	nd	nd	3.02 (2.14)	1.79 (0.93)	1.00	0.75 (0.04)	9.28 (1.76)	3.20 (0.57)	17.3 (12.0)	3.96 (2.97)	8.53 (3.92)	29.0 (16.3)	37.9 (26.7)	10.1 (7.4)	136 (42)	191 (15)
20f	nd	nd	2.41 (1.56)	0.59 (0.64)	1.00	0.89 (0.03)	3.04 (1.37)	1.60 (0.39)	17.3 (9.3)	*1.8*	3.55 (2.29)	47.9 (12.7)	30.3 (20.8)	*5.2*	*31.6*	149 (12)
20j	nd	nd	3.57 (1.43)	1.65 (0.63)	1.00	0.96 (0.02)	2.83 (0.97)	2.00 (0.38)	7.68 (6.63)	4.55 (1.97)	5.96 (2.17)	16.9 (9.0)	29.7 (14.8)	5.2 (4.1)	70.7 (23.2)	64.8 (8.6)
20k	nd	nd	2.97 (0.22)	1.94 (0.10)	1.00	0.01 (0.00)	*0.4*	0.24 (0.05)	*3*	*0.6*	1.44 (0.38)	13.2 (2.1)	*6.7*	3.2 (0.5)	*10.3*	10.6 (1.0)
20l	nd	nd	5.16 (2.19)	2.12 (0.95)	1.00	0.51 (0.03)	10.4 (1.8)	4.94 (0.58)	46.1 (14.8)	*5.1*	*15.1*	*40.9*	*88*	*18.2*	*209*	241 (19)
20m	11.7 (0.5)	0.91 (0.24)	1.85 (0.21)	2.14 (0.29)	1.00	2.51 (0.05)	*56*	*23*	*305*	nd	nd	nd	nd	nd	nd	nd
20n	3.41 (0.13)	1.08 (0.08)	1.72 (0.11)	1.52 (0.08)	1.00	0.67 (0.01)	*20*	*8*	*66*	nd	nd	nd	nd	nd	nd	nd
20o	9.55 (0.33)	1.41 (0.21)	2.85 (0.15)	4.67 (0.20)	1.00	0.91 (0.04)	*51*	*17*	*159*	nd	nd	nd	nd	nd	nd	nd
20p	14.8 (0.5)	1.81 (0.27)	3.89 (0.23)	5.33 (0.33)	1.00	1.23 (0.06)	*76*	*22*	*329*	nd	nd	nd	nd	nd	nd	nd
20q	245 (9)	44.1 (3.8)	41.9 (3.3)	31.4 (4.6)	1.00	6.01 (0.80)	*1271*	*386*	*4106*	nd	nd	nd	nd	nd	nd	nd

Table 3c.

	Elemental abundances (Fe- and CI-normalized)															
	S	Ca	Cr	Mn	Fe	Ni	Cu	Zn	Ga	Ge	Se	Br	Rb	Sr	Y	Zr
Track C2115,21																
21a	nd	nd	1.44 (0.11)	1.65 (0.05)	1.00	0.93 (0.002)	0.66 (0.08)	0.18 (0.02)	11.7 (0.5)	2.03 (0.12)	2.59 (0.13)	2.88 (0.74)	5.02 (1.21)	1.50 (0.34)	4.69 (1.90)	1.30 (0.70)
21b	nd	nd	0.70 (0.14)	1.14 (0.07)	1.00	0.28 (0.002)	0.16 (0.09)	0.08 (0.03)	3.59 (0.63)	*0.3*	2.11 (0.18)	*0.3*	*1.8*	*0.7*	*1.8*	*1.5*
21c	nd	nd	0.49 (0.16)	0.68 (0.08)	1.00	0.64 (0.004)	0.33 (0.11)	4.49 (0.05)	1.98 (0.84)	*0.3*	2.55 (0.26)	*0.4*	*0.9*	*0.5*	*1.7*	*1.0*
21d	nd	nd	1.10 (0.15)	0.89 (0.07)	1.00	0.19 (0.002)	0.48 (0.10)	0.18 (0.03)	4.77 (0.78)	*0.7*	2.88 (0.19)	*1.5*	*4.1*	*1.3*	*6.4*	*2.7*
21e	0.32 (0.01)	1.59 (0.01)	1.81 (0.03)	2.35 (0.02)	1.00	0.73 (0.002)	1.39 (0.05)	0.35 (0.01)	8.40 (0.28)	*0.07*	1.34 (0.07)	*0.2*	2.00 (0.63)	0.66 (0.12)	*1.0*	0.58 (0.36)
21f	nd	nd	1.60 (0.07)	2.27 (0.04)	1.00	0.46 (0.002)	0.49 (0.05)	0.14 (0.01)	6.25 (0.37)	0.20 (0.07)	1.79 (0.09)	1.05 (0.51)	3.57 (0.83)	0.80 (0.23)	*0.97*	0.70 (0.48)
21g	0.25 (0.01)	1.10 (0.01)	4.05 (0.05)	4.27 (0.03)	1.00	0.54 (0.002)	1.17 (0.05)	0.30 (0.01)	10.6 (0.4)	*0.0*	1.08 (0.13)	0.82 (0.55)	2.21 (0.90)	0.24 (0.21)	*0.5*	*0.1*
21h	nd	nd	5.30 (0.35)	7.19 (0.16)	1.00	0.25 (0.04)	*0.22*	0.32 (0.07)	15.1 (1.8)	*0.3*	*0.6*	*0.1*	*1.1*	*0.3*	*1.1*	*0.4*
21i	nd	nd	*0.65*	*0.27*	1.00	0.05 (0.01)	1.38 (0.43)	8.87 (0.14)	*2.32*	*1.3*	*1.1*	*0.2*	*1.7*	*0.4*	*5.5*	*1.8*
21j	*1.6*	3.12 (0.04)	4.48 (0.05)	4.31 (0.03)	1.00	0.69 (0.01)	8.49 (0.26)	3.64 (0.08)	65.7 (3.3)	nd	nd	nd	nd	nd	nd	nd
21k	*1.4*	2.09 (0.06)	2.87 (0.06)	4.41 (0.08)	1.00	0.84 (0.01)	12.81 (0.48)	4.78 (0.15)	56.1 (4.1)	nd	nd	nd	nd	nd	nd	nd
21l	0.39 (0.01)	0.33 (0.01)	0.56 (0.01)	1.29 (0.02)	1.00	0.90 (0.003)	2.00 (0.05)	4.43 (0.02)	6.78 (0.39)	nd	nd	nd	nd	nd	nd	nd
21m	0.44 (0.01)	1.31 (0.01)	1.83 (0.01)	2.29 (0.02)	1.00	1.24 (0.003)	2.60 (0.09)	0.94 (0.03)	18.2 (0.5)	nd	nd	nd	nd	nd	nd	nd
21n	*0.9*	0.59 (0.03)	0.81 (0.03)	1.41 (0.04)	1.00	0.77 (0.01)	5.53 (0.25)	5.06 (0.10)	21.0 (1.8)	nd	nd	nd	nd	nd	nd	nd
21o	*1.2*	1.14 (0.06)	1.46 (0.05)	1.88 (0.07)	1.00	1.22 (0.01)	11.0 (0.6)	5.85 (0.20)	35.0 (3.6)	nd	nd	nd	nd	nd	nd	nd
21p	11.9 (0.5)	41.5 (0.6)	5.90 (0.24)	4.09 (0.33)	1.00	1.45 (0.06)	141 (5)	2566 (8)	402 (32)	nd	nd	nd	nd	nd	nd	nd
21q	*0.9*	2.90 (0.04)	3.60 (0.02)	4.51 (0.03)	1.00	0.63 (0.005)	6.37 (0.30)	1.01 (0.08)	62.3 (2.6)	nd	nd	nd	nd	nd	nd	nd

Table 3d.

	Elemental abundances (Fe- and CI-normalized)															
	S	Ca	Cr	Mn	Fe	Ni	Cu	Zn	Ga	Ge	Se	Br	Rb	Sr	Y	Zr
Track C2115,22																
22aa	0.02 (0.002)	2.71 (0.01)	2.46 (0.01)	2.40 (0.01)	1.00	0.04 (0.001)	0.07 (0.01)	0.40 (0.01)	32.6 (0.0)	*0.03*	0.04 (0.03)	*0.14*	2.45 (0.26)	0.36 (0.06)	2.33 (0.32)	0.68 (0.12)
22a	nd	nd	1.40 (1.10)	1.83 (0.37)	1.00	0.04 (0.003)	*0.10*	0.60 (0.03)	51.9 (0.1)	*0.10*	0.28 (0.09)	*0.37*	5.48 (0.60)	0.44 (0.17)	6.02 (0.83)	2.36 (0.30)
22b	nd	nd	2.08 (1.07)	1.50 (0.36)	1.00	0.08 (0.003)	0.24 (0.10)	0.19 (0.02)	10.8 (0.5)	0.09 (0.09)	0.74 (0.06)	0.42 (0.45)	1.20 (0.37)	0.28 (0.15)	1.92 (0.58)	0.75 (0.21)
22c	nd	nd	1.29 (0.40)	1.91 (0.14)	1.00	0.03 (0.001)	*0.03*	0.11 (0.01)	3.91 (0.18)	*0.03*	1.25 (0.02)	*0.14*	0.65 (0.12)	0.10 (0.05)	1.05 (0.18)	0.38 (0.07)
22d	0.03 (0.003)	0.14 (0.003)	0.94 (0.30)	2.09 (0.11)	1.00	0.02 (0.001)	0.18 (0.03)	0.22 (0.01)	5.56 (0.27)	*0.05*	0.56 (0.03)	0.33 (0.22)	0.78 (0.18)	0.10 (0.08)	0.99 (0.29)	0.46 (0.32)
22e	0.03 (0.002)	0.23 (0.004)	1.03 (0.28)	2.48 (0.10)	1.00	0.04 (0.001)	0.16 (0.05)	0.43 (0.01)	62.9 (0.9)	0.03 (0.08)	0.35 (0.08)	*0.36*	3.04 (0.50)	0.40 (0.14)	1.25 (0.78)	0.71 (0.10)
22f	nd	nd	2.21 (0.79)	1.75 (0.25)	1.00	0.02 (0.002)	0.12 (0.08)	0.07 (0.02)	9.62 (0.34)	0.12 (0.07)	0.40 (0.07)	0.60 (0.26)	1.12 (0.43)	0.27 (0.12)	1.02 (0.68)	0.92 (0.25)
22g	nd	nd	1.15 (0.58)	1.49 (0.20)	1.00	0.04 (0.001)	0.10 (0.04)	0.82 (0.02)	2.45 (0.18)	0.06 (0.05)	0.30 (0.04)	0.23 (0.14)	0.98 (0.23)	*0.10*	0.99 (0.36)	0.60 (0.13)
22h	nd	nd	3.74 (1.33)	1.21 (0.43)	1.00	0.03 (0.003)	0.13 (0.13)	0.10 (0.03)	12.6 (0.6)	*0.12*	0.64 (0.12)	0.77 (0.45)	0.87 (0.74)	*0.21*	1.36 (1.17)	1.99 (0.86)
22i	nd	nd	2.40 (0.96)	1.81 (0.32)	1.00	0.03 (0.002)	0.09 (0.09)	0.20 (0.02)	6.81 (0.47)	0.08 (0.07)	0.29 (0.08)	0.26 (0.15)	1.29 (0.50)	0.24 (0.14)	1.62 (0.39)	0.61 (0.14)
22j	nd	nd	1.83 (0.62)	0.81 (0.21)	1.00	0.02 (0.001)	0.09 (0.06)	0.07 (0.01)	1.92 (0.26)	0.14 (0.06)	0.75 (0.05)	0.38 (0.20)	0.52 (0.33)	0.18 (0.09)	0.75 (0.52)	0.62 (0.19)
22k	nd	nd	1.66 (0.89)	1.01 (0.29)	1.00	0.01 (0.001)	0.12 (0.09)	0.06 (0.02)	0.57 (0.39)	0.14 (0.08)	0.65 (0.08)	0.49 (0.30)	0.94 (0.50)	*0.14*	0.80 (0.78)	1.01 (0.86)
22l	nd	nd	2.00 (1.92)	1.32 (0.64)	1.00	0.03 (0.004)	*0.18*	0.59 (0.05)	33.8 (1.4)	*0.15*	0.50 (0.16)	*0.70*	2.61 (1.14)	0.69 (0.32)	1.97 (0.51)	1.42 (0.19)
22m	nd	nd	2.50 (1.05)	0.77 (0.35)	1.00	0.21 (0.003)	0.44 (0.11)	0.04 (0.02)	1.63 (0.47)	0.09 (0.10)	2.90 (0.10)	1.43 (0.37)	2.20 (0.60)	0.29 (0.17)	0.83 (0.95)	1.47 (0.35)
22n	nd	nd	8.51 (4.82)	2.24 (1.44)	1.00	1.09 (0.02)	3.18 (0.49)	0.34 (0.10)	3.31 (2.17)	5.73 (0.46)	4.12 (0.46)	2.65 (1.69)	7.09 (2.76)	0.67 (0.77)	3.64 (4.34)	7.73 (1.60)
22o	nd	nd	7.93 (4.06)	1.59 (1.21)	1.00	0.96 (0.01)	3.42 (0.41)	0.31 (0.08)	3.39 (1.83)	1.43 (0.39)	4.01 (0.38)	1.86 (1.42)	4.98 (2.33)	1.26 (0.65)	4.25 (3.66)	5.58 (1.35)
22p	nd	nd	4.63 (2.73)	1.65 (0.82)	1.00	0.92 (0.01)	2.68 (0.28)	0.11 (0.06)	*1.23*	0.42 (0.26)	3.23 (0.26)	1.60 (0.96)	2.15 (1.56)	0.39 (0.44)	*2.46*	5.22 (0.91)
22r	nd	nd	632 (490)	165 (147)	1.00	2.22 (0.84)	114 (49)	9117 (40)	616 (221)	*67.2*	*92*	19,438 (172)	3483 (281)	95 (78)	*442*	1092 (163)
22s	nd	nd	26.3 (12.9)	8.06 (3.86)	1.00	0.75 (0.03)	3.45 (1.30)	30.8 (0.5)	17.5 (5.8)	2.72 (1.23)	6.12 (1.22)	9.00 (4.52)	24.8 (7.4)	3.75 (2)	15.5 (11.6)	15.8 (4.3)
22t	nd	nd	2.14 (0.41)	1.72 (0.16)	1.00	0.02 (0.001)	*0.04*	0.27 (0.01)	9.03 (0.19)	0.02 (0.04)	0.45 (0.04)	0.24 (0.14)	1.51 (0.24)	0.33 (0.07)	1.84 (0.37)	0.56 (0.14)
22u	nd	nd	7.09 (5.47)	3.55 (1.64)	1.00	0.08 (0.01)	0.73 (0.55)	0.18 (0.11)	62.5 (2.47)	*0.52*	0.52 (0.52)	1.65 (1.92)	4.66 (3.14)	0.98 (0.87)	*4.93*	1.94 (1.82)
22v	0.20 (0.01)	0.19 (0.01)	1.76 (0.01)	1.44 (0.02)	1.00	0.02 (0.001)	0.83 (0.07)	0.28 (0.02)	7.45 (0.89)	*0.19*	0.18 (0.19)	*0.69*	1.80 (1.13)	*0.32*	2.16 (1.78)	0.66 (0.66)
22w	0.03 (0.001)	1.19 (0.002)	1.61 (0.003)	2.81 (0.004)	1.00	0.05 (0.001)	0.08 (0.01)	0.49 (0.001)	36.5 (6.7)	nd	nd	nd	nd	nd	nd	nd
22x	0.42 (0.02)	0.51 (0.01)	0.87 (0.01)	1.08 (0.02)	1.00	0.63 (0.004)	3.73 (0.10)	0.98 (0.03)	11.4 (0.9)	nd	nd	nd	nd	nd	nd	nd

Table 3e.

	Elemental abundances (Fe- and CI-normalized)							
	S	Ca	Cr	Mn	Fe	Ni	Cu	Zn
Track C2044,~~12~~ 1								
~~12~~ 1a	0.03 (0.001)	*0.0*	0.87 (0.003)	0.21 (0.001)	1.00	1.55 (0.17)	*0.8*	*0.0*
~~12~~ 1b	0.17 (0.01)	*0.1*	1.14 (0.04)	*0.1*	1.00	1.96 (0.77)	8.54 (0.26)	*0.3*
~~12~~ 1c	*0.1*	*0.2*	1.30 (0.05)	*0.3*	1.00	1.96 (0.03)	14.0 (0.5)	2.02 (0.12)
~~12~~ 1d	*0.1*	*0.2*	1.36 (0.04)	*0.3*	1.00	2.21 (0.03)	12.0 (0.5)	2.05 (0.10)
~~12~~ 1e	*0.1*	*0.3*	1.00 (0.07)	*0.4*	1.00	2.03 (0.13)	15.8 (0.8)	3.47 (0.17)
~~12~~ 1f	*0.3*	*0.3*	1.73 (0.07)	*0.4*	1.00	2.08 (0.04)	17.0 (0.8)	*2.7*
~~12~~ 1g	1.44 (0.10)	*1.3*	*1.4*	*1.7*	1.00	1.94 (0.17)	*44.3*	*9.4*
~~12~~ 1h	*0.3*	*0.6*	*2.2*	*0.8*	1.00	1.99 (0.08)	*23.6*	*1.8*
~~12~~ 1i	0.38 (0.02)	*0.5*	1.43 (0.07)	*0.6*	1.00	1.95 (0.12)	*14.0*	*1.4*
~~12~~ 1j	*0.1*	*0.2*	1.44 (0.03)	*0.2*	1.00	2.34 (0.10)	9.29 (0.36)	1.37 (0.08)
~~12~~ 1k	0.14 (0.01)	*0.1*	1.29 (0.03)	*0.2*	1.00	2.06 (0.03)	6.09 (0.29)	0.97 (0.06)
~~12~~ 1l	*0.1*	*0.2*	1.13 (0.04)	*0.2*	1.00	2.06 (0.02)	*7.9*	*1.1*
~~12~~ 1m	*0.2*	*0.2*	1.48 (0.04)	*0.3*	1.00	2.13 (0.05)	9.32 (0.38)	*1.3*
~~12~~ 1n	*0.1*	*0.2*	1.16 (0.03)	*0.2*	1.00	2.08 (0.02)	*6.0*	*0.9*
~~12~~ 1o	*0.1*	*0.2*	1.25 (0.04)	*0.3*	1.00	2.04 (0.03)	6.65 (0.31)	1.25 (0.10)
~~12~~ 1p	*0.1*	*0.2*	1.20 (0.05)	*0.3*	1.00	2.17 (0.03)	*7.2*	*1.1*
~~12~~ 1q	*0.2*	*0.4*	4.54 (0.08)	*0.5*	1.00	1.41 (0.05)	*3.8*	*1.1*
~~12~~ 1r	*0.2*	*0.4*	3.30 (0.33)	*0.5*	1.00	2.01 (0.05)	*3.8*	*1.1*

Table 3f.

	Elemental abundances (Fe- and CI-normalized)								
	S	Ca	Cr	Mn	Fe	Ni	Cu	Zn	Ga
Track C2044,~~7~~ 1									
~~7~~ 1a	*0.1*	0.46 (0.01)	0.89 (0.02)	0.37 (0.02)	1.00	1.13 (0.05)	3.83 (0.12)	1.31 (0.04)	12.1 (2.4)
~~7~~ 1b	0.13 (0.01)	0.47 (0.01)	0.72 (0.02)	0.41 (0.02)	1.00	1.14 (0.05)	4.77 (0.14)	1.98 (0.04)	*1.9*
~~7~~ 1c	0.20 (0.01)	1.09 (0.02)	1.97 (0.02)	2.53 (0.03)	1.00	1.09 (0.05)	4.40 (0.13)	2.68 (0.04)	*2.0*
~~7~~ 1d	0.08 (0.003)	0.74 (0.01)	0.61 (0.01)	0.57 (0.01)	1.00	1.08 (0.03)	2.98 (0.09)	0.65 (0.02)	2.13 (0.42)
~~7~~ 1e	0.13 (0.01)	0.46 (0.01)	0.72 (0.01)	0.38 (0.01)	1.00	1.15 (0.03)	3.14 (0.09)	0.86 (0.03)	*0.9*
~~7~~ 1f	0.22 (0.01)	0.53 (0.01)	0.73 (0.02)	0.43 (0.02)	1.00	1.08 (0.05)	4.17 (0.12)	2.61 (0.05)	*2.2*

Table 3g.

	Elemental abundances (Fe- and CI-normalized)								
	S	Ca	Cr	Mn	Fe	Ni	Cu	Zn	Ga
Track C2027,48									
48-1a	9.03 (0.61)	1420 (4.54)	13.2 (1.6)	*5.7*	1.00	24.0 (0.2)	925 (18)	5437 (19)	*366*
48-1b	*5.1*	1668 (8)	*27*	*17*	1.00	2.36 (0.48)	2048 (53)	216 (11)	*1078*
48-1c	*1.4*	137 (2)	*9.5*	*4.6*	1.00	4.70 (0.13)	615 (15)	1218 (6)	*299*
48-1d	*0.7*	384 (2)	5.62 (0.64)	*2.3*	1.00	1.62 (0.09)	395 (7)	19138 (16)	*149*
48-1e	8.16 (0.20)	167 (1)	4.40 (0.45)	*3.0*	1.00	1.75 (0.05)	269 (5)	6197 (11)	*104*
48-1f	*0.2*	0.76 (0.06)	1.61 (0.07)	*1.6*	1.00	1.56 (0.01)	32.6 (0.8)	*1.2*	*16*
48-1g	*0.1*	0.83 (0.02)	1.47 (0.04)	1.34 (0.05)	1.00	1.25 (0.01)	17.2 (0.4)	0.67 (0.10)	*9.1*
48-1h	*0.04*	*0.23*	0.60 (0.04)	2.13 (0.05)	1.00	0.05 (0.004)	15.3 (0.4)	1.40 (0.10)	*9.0*
48-1i	0.20 (0.002)	0.05 (0.004)	0.24 (0.004)	0.37 (0.005)	1.00	0.22 (0.001)	1.53 (0.04)	0.14 (0.01)	*0.8*
48-1j	*0.02*	0.23 (0.003)	0.91 (0.01)	2.46 (0.01)	1.00	0.10 (0.001)	1.31 (0.03)	0.14 (0.01)	3.77 (0.22)

Table 3g. *Continued.*

	Elemental abundances (Fe- and CI-normalized)								
	S	Ca	Cr	Mn	Fe	Ni	Cu	Zn	Ga
48-1k	0.06 (0.004)	0.73 (0.01)	1.28 (0.01)	1.50 (0.02)	1.00	1.09 (0.004)	5.72 (0.13)	0.45 (0.03)	*2.6*
48-1l	0.06 (0.002)	0.71 (0.01)	1.35 (0.01)	1.64 (0.01)	1.00	1.08 (0.001)	3.49 (0.06)	0.14 (0.01)	*1.3*
48-1m	0.07 (0.003)	0.78 (0.01)	1.41 (0.01)	1.57 (0.01)	1.00	1.01 (0.003)	5.47 (0.10)	1.24 (0.02)	*2.0*
48-1n	0.05 (0.002)	0.65 (0.01)	1.29 (0.02)	1.88 (0.01)	1.00	0.93 (0.002)	3.82 (0.06)	0.82 (0.01)	*2.2*
48-1o	*0.03*	0.51 (0.01)	1.07 (0.01)	1.98 (0.01)	1.00	0.74 (0.002)	3.97 (0.08)	1.04 (0.02)	*3.4*
48-1p	0.09 (0.004)	1.18 (0.02)	1.39 (0.01)	1.51 (0.01)	1.00	1.15 (0.004)	6.10 (0.12)	3.46 (0.03)	*3.6*
48-1q	0.08 (0.005)	0.84 (0.01)	1.39 (0.01)	1.46 (0.02)	1.00	1.35 (0.004)	7.01 (0.14)	1.20 (0.03)	*2.9*
48-1r	*0.2*	1.20 (0.02)	1.47 (0.04)	1.53 (0.06)	1.00	1.23 (0.007)	16.8 (0.5)	3.84 (0.10)	*9.4*
48-1s	0.14 (0.01)	0.77 (0.01)	1.40 (0.02)	1.34 (0.03)	1.00	1.25 (0.01)	9.85 (0.22)	2.86 (0.05)	*4.5*
48-1t	0.13 (0.005)	0.67 (0.01)	1.02 (0.01)	1.19 (0.02)	1.00	1.28 (0.004)	6.54 (0.14)	0.78 (0.03)	*2.8*
48-1u	0.27 (0.01)	*0.05*	*0.2*	*0.1*	1.00	0.15 (0.002)	6.02 (0.18)	0.62 (0.04)	*3.7*
48-1v	0.13 (0.01)	0.92 (0.02)	4.65 (0.04)	5.67 (0.02)	1.00	0.81 (0.005)	6.71 (0.15)	1.93 (0.03)	*3.1*
48-1w	0.19 (0.01)	0.57 (0.02)	0.96 (0.02)	0.97 (0.02)	1.00	0.94 (0.005)	6.87 (0.16)	1.47 (0.03)	*3.2*
48-1x	0.10 (0.004)	0.91 (0.01)	2.16 (0.01)	1.63 (0.01)	1.00	1.17 (0.003)	5.19 (0.11)	0.76 (0.02)	*2.2*
48-1y	0.07 (0.003)	0.88 (0.01)	1.43 (0.01)	1.57 (0.01)	1.00	1.09 (0.001)	4.50 (0.08)	0.33 (0.02)	*1.5*
48-1z	*0.1*	0.80 (0.03)	1.87 (0.03)	1.61 (0.03)	1.00	1.35 (0.007)	8.79 (0.24)	1.07 (0.05)	*4.8*
48-1aa	0.17 (0.01)	0.96 (0.02)	1.43 (0.03)	1.46 (0.03)	1.00	1.34 (0.01)	8.24 (0.21)	0.74 (0.05)	*4.4*
48-1ab	0.08 (0.002)	0.59 (0.01)	1.75 (0.01)	1.15 (0.01)	1.00	1.17 (0.003)	4.00 (0.10)	0.15 (0.02)	*1.9*
48-1ac	*0.01*	0.49 (0.01)	1.61 (0.01)	1.46 (0.01)	1.00	1.18 (0.003)	4.25 (0.09)	0.30 (0.02)	7.54 (0.60)
48-1ad	*0.04*	0.70 (0.01)	1.67 (0.01)	2.07 (0.01)	1.00	1.58 (0.004)	5.14 (0.12)	0.30 (0.02)	*2.4*
48-1ae	*0.03*	0.52 (0.01)	1.68 (0.04)	1.46 (0.04)	1.00	1.34 (0.01)	12.6 (0.3)	2.13 (0.07)	*9.7*
48-1af	*0.06*	0.75 (0.03)	1.51 (0.03)	1.61 (0.03)	1.00	1.09 (0.01)	8.52 (0.22)	1.18 (0.05)	*4.5*
48-2a	*0.01*	0.65 (0.003)	1.66 (0.01)	2.38 (0.005)	1.00	0.18 (0.001)	0.67 (0.01)	0.13 (0.003)	3.69 (0.09)
48-2b	*0.001*	0.18 (0.001)	2.76 (0.004)	2.46 (0.004)	1.00	0.07 (0.001)	0.19 (0.01)	0.06 (0.002)	3.40 (0.06)
48-2c	*0.001*	0.07 (0.001)	0.95 (0.000)	2.35 (0.005)	1.00	0.04 (0.001)	*0.1*	0.05 (0.002)	*0.2*
48-2d	0.03 (0.002)	*0.01*	*0.1*	0.40 (0.001)	1.00	0.30 (0.001)	0.93 (0.03)	6.09 (0.05)	*1.0*
48-2e	*0.04*	0.49 (0.03)	2.08 (0.04)	1.16 (0.06)	1.00	1.05 (0.01)	3.83 (0.31)	5.90 (0.10)	*9.5*
48-3a	0.15 (0.01)	0.62 (0.01)	0.99 (0.02)	1.25 (0.02)	1.00	1.35 (0.01)	2.60 (0.13)	2.70 (0.04)	*3.9*
48-3b	0.18 (0.01)	0.98 (0.03)	1.08 (0.04)	1.18 (0.05)	1.00	1.26 (0.01)	2.93 (0.14)	5.05 (0.09)	*8.5*
48-3c	0.15 (0.01)	0.89 (0.03)	1.76 (0.03)	1.65 (0.05)	1.00	1.50 (0.01)	2.32 (0.13)	4.64 (0.08)	*8.0*
48-3d	0.14 (0.01)	0.76 (0.02)	0.95 (0.03)	2.81 (0.04)	1.00	3.48 (0.01)	4.04 (0.10)	2.99 (0.06)	*5.9*
48-3e	*0.13*	0.73 (0.04)	0.81 (0.05)	1.67 (0.07)	1.00	1.18 (0.01)	2.46 (0.19)	4.58 (0.06)	*11.6*
48-3f	0.14 (0.005)	0.68 (0.02)	1.33 (0.02)	1.31 (0.03)	1.00	1.02 (0.01)	2.00 (0.07)	1.38 (0.02)	*4.4*
48-3g	*0.09*	0.54 (0.03)	2.94 (0.03)	0.89 (0.04)	1.00	1.42 (0.01)	3.64 (0.12)	2.27 (0.04)	*7.1*
48-3h	*0.02*	0.16 (0.01)	0.48 (0.01)	2.31 (0.01)	1.00	0.11 (0.001)	0.41 (0.03)	0.81 (0.01)	*2.0*
48-3i	0.06 (0.002)	0.83 (0.005)	1.70 (0.01)	3.01 (0.01)	1.00	1.20 (0.002)	2.63 (0.04)	0.78 (0.01)	*1.4*
48-3j	*0.17*	0.59 (0.03)	1.49 (0.03)	1.09 (0.05)	1.00	0.92 (0.01)	3.00 (0.25)	3.84 (0.08)	*7.6*
48-3k	0.07 (0.01)	0.99 (0.02)	1.60 (0.03)	1.37 (0.04)	1.00	1.07 (0.01)	4.95 (0.20)	3.63 (0.06)	*6.2*
48-3l	*0.02*	0.76 (0.02)	1.33 (0.02)	1.48 (0.03)	1.00	1.22 (0.01)	2.51 (0.15)	2.77 (0.05)	*4.6*
48-3m	0.14 (0.003)	0.99 (0.01)	1.60 (0.01)	1.55 (0.02)	1.00	1.08 (0.005)	2.27 (0.10)	1.21 (0.02)	*3.1*
48-3n	*0.06*	0.75 (0.04)	2.04 (0.05)	1.50 (0.07)	1.00	0.86 (0.01)	*1.6*	5.86 (0.07)	*12.4*
48-3o	0.12 (0.004)	0.92 (0.01)	1.51 (0.01)	1.55 (0.01)	1.00	1.29 (0.003)	2.74 (0.07)	1.12 (0.02)	*2.3*
48-3p	0.19 (0.01)	0.92 (0.01)	1.23 (0.02)	1.43 (0.02)	1.00	1.09 (0.01)	2.67 (0.13)	3.40 (0.04)	*4.1*
48-3q	*0.18*	1.07 (0.03)	1.50 (0.04)	1.66 (0.05)	1.00	1.18 (0.01)	*3.2*	6.18 (0.09)	*8.6*
48-3r	*0.03*	0.53 (0.03)	2.59 (0.03)	2.98 (0.04)	1.00	0.93 (0.01)	*2.2*	4.01 (0.08)	*7.4*

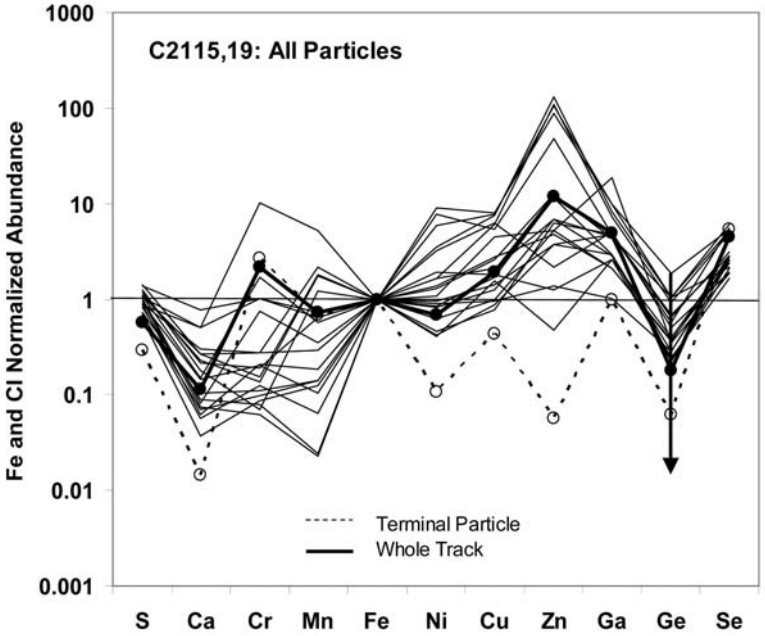

Fig. 5. Elemental abundance patterns obtained at the APS for 20 particles on C2115,19, an 860 μm long track. The CI- and Fe-normalized element abundances for the terminal particle (TP) and the most intense element hot spots are plotted along with the whole-track average composition, determined by adding the element abundances from spot analyses along the track and the analysis of the terminal particle. The horizontal line at 1 is the CI meteorite composition, which is thought to represent the mean solar system composition. The vertical arrow indicates that all Ge analyses for these particles except the TP were upper limits (after Flynn et al. 2006, Fig. 1).

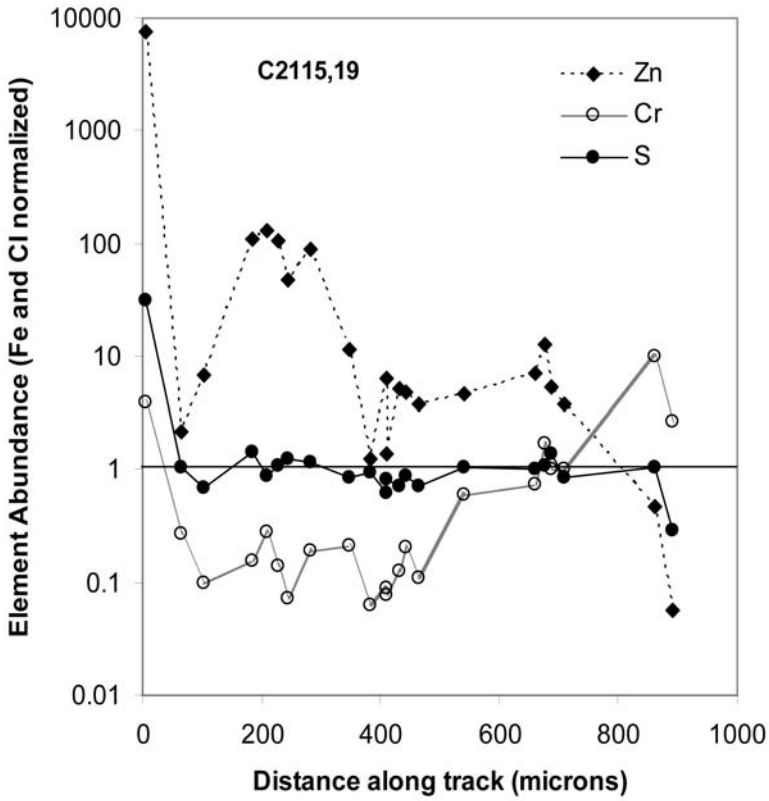

Fig. 6. Chromium, Zn, and S elemental abundances for individual particles as a function of distance from the track entry point for C2115,19. Zinc shows a decrease with distance, whereas Cr shows an increase and S is relatively uniform.

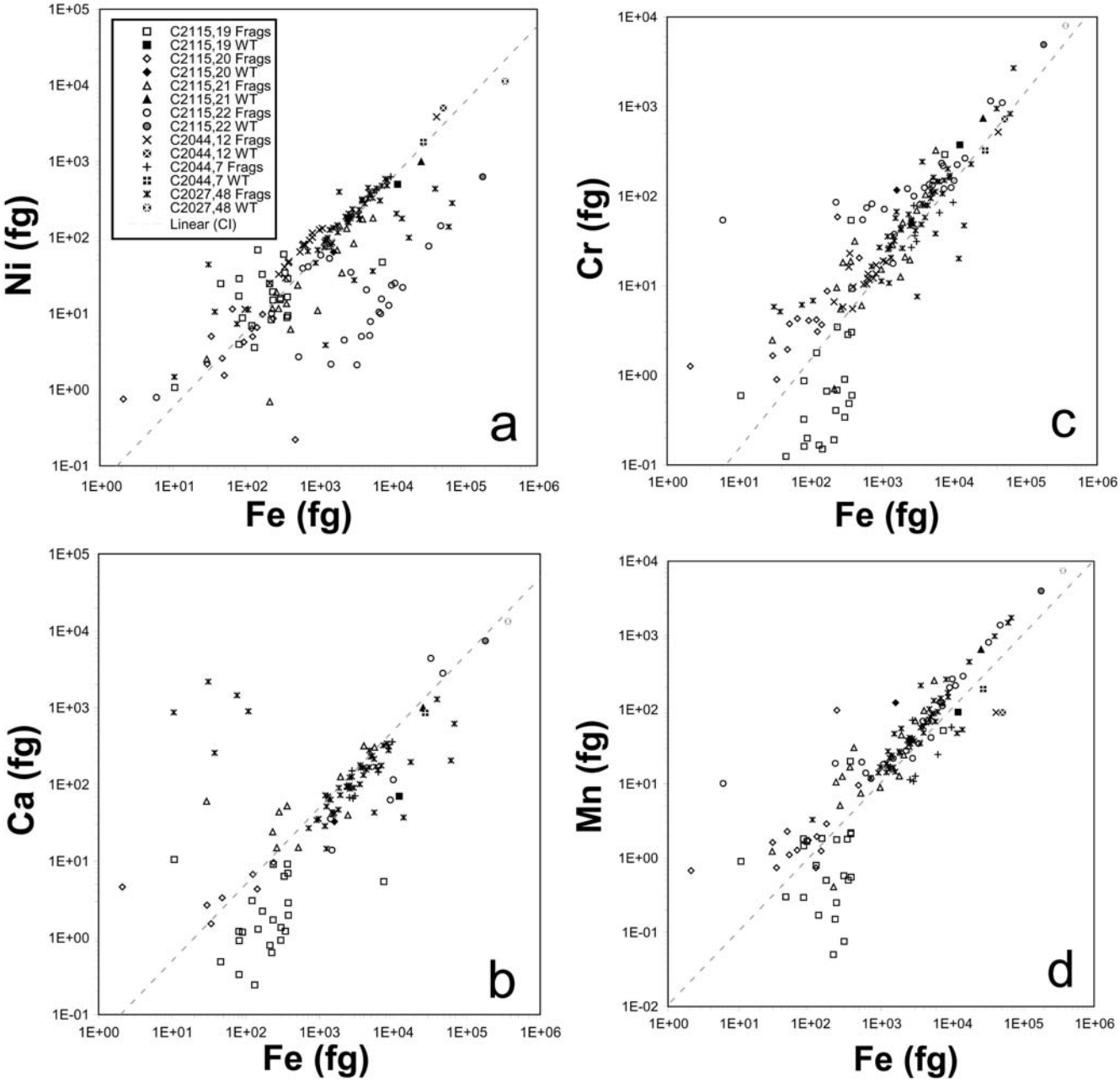

Fig. 7. a–d) Element abundances versus Fe abundance for Ni, Ca, Cr, Mn, Cu, Ga, Zn, and S in all 156 individual particles and whole track values. Data symbols are grouped according to track affiliation. The dashed diagonal lines correspond to the element/Fe ratio in CI meteorites.

C2044,22 have Ni/Fe ratios substantially lower than CI and possibly lower Cu/Fe and Zn/Fe. As a group, all the fragment analyses display greater spread in Cu/Fe and Zn/Fe about the CI composition. Ga/Fe ratios for almost all the fragments are enriched relative to CI. Selected fragments from track C2115,22 are particularly enriched in Ga. Flynn et al. (2006) note that overall the tracks analyzed show enrichments in the moderately volatile elements Cu, Zn, and Ga relative to CI, similar to what is observed in interplanetary dust particles (IDPs), but also note that these elements are not well-determined in the solar photosphere. S/Fe in most of the fragments is depleted relative to CI. IDPs show similar depletions in S relative to CI. However, the loss in S could potentially result from volatilization during aerogel capture.

The seven tracks show some variation in fragment heterogeneity, which can be seen by observing the range of abundance values in each element in Tables 3a–g. First of all, it can be seen that the variation in Fe and CI normalized abundances can be quite large, up to 10^5 in some cases. Cr/Fe,

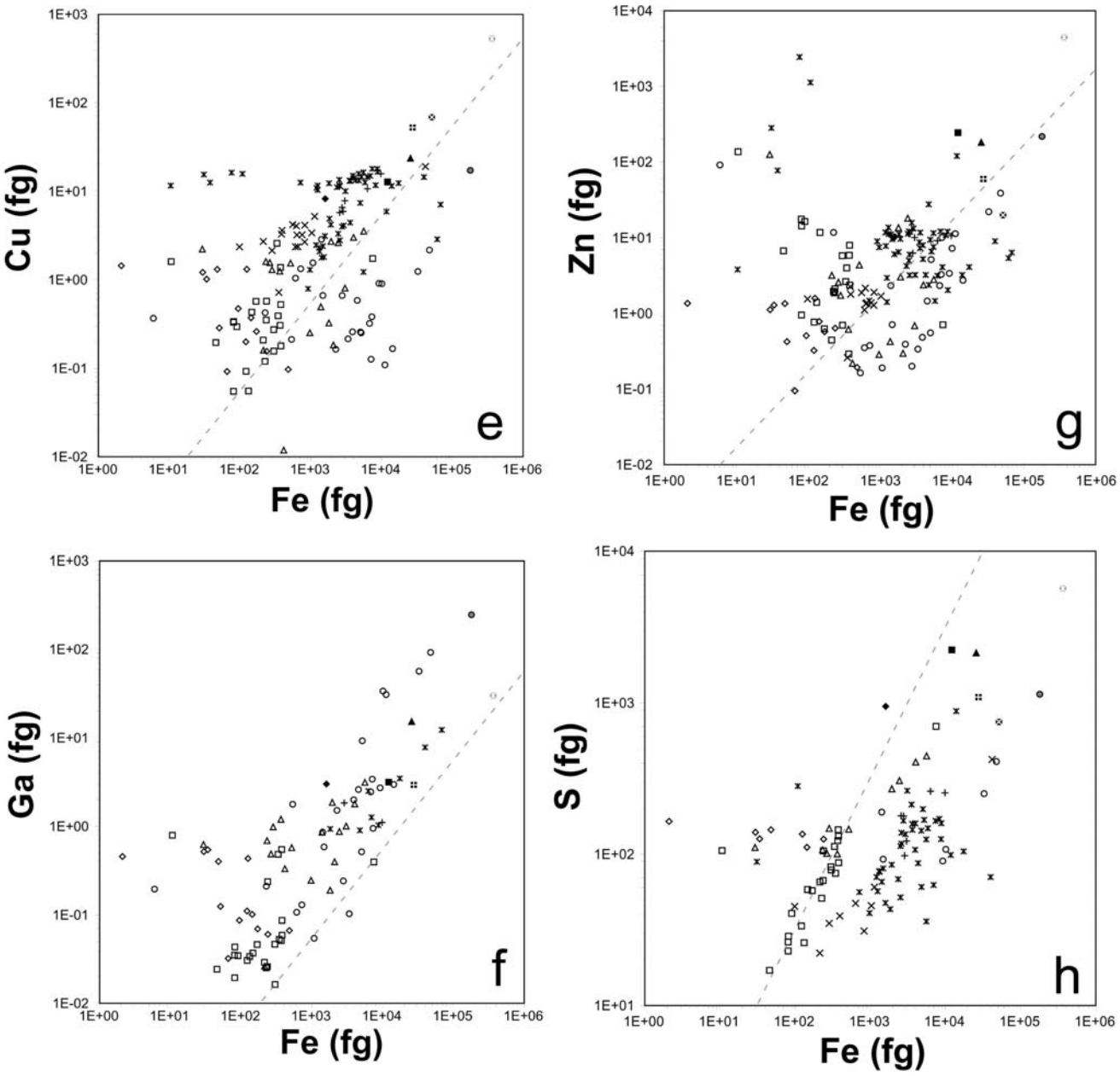

Fig. 7. e–h) *Continued.* Element abundances versus Fe abundance for Ni, Ca, Cr, Mn, Cu, Ga, Zn, and S in all 156 individual particles and whole track values. Data symbols are grouped according to track affiliation. The dashed diagonal lines correspond to the element/Fe ratio in CI meteorites.

Mn/Fe, and Ni/Fe show the tightest distributions, which is consistent with the observation that these elements are fairly well correlated (Figs. 7a, 7c, and 7d). Calcium, Cu, and Zn are the most diverse, again consistent with the generally scattered appearance of plots of these elements versus Fe (Figs. 7a, 7e, and 7g).

C2027,48 has the largest abundance ranges, whereas C2044,7 has the smallest, suggesting that they are the least and most homogeneous, respectively. However, the abundance ranges are only part of the story and can be affected by rare fragments of unusual composition. Figure 7 gives a detailed view of the abundance distributions. Nickel is close to CI in all tracks, with the exception of C2115,22, which shows a bi-modal distribution. One mode is at CI and the other is about an order of magnitude lower. The latter undoubtedly represents crystalline fragments where Fe-Ni partitioning has occurred. This is consistent with the fact that the terminal particle for this track was largely olivine (Zolensky et al. 2006). Evidence of this low-Ni mode can be seen in the Ni-abundance distribution for most of the other

Table 4a. Correlation coefficients: track C2115,19.

	S	Ca	Cr	Mn	Fe	Ni	Cu	Zn	Ga	Se
S	1.00									
Ca	0.40	1.00								
Cr	**0.97**	0.25	1.00							
Mn	**0.94**	0.33	**0.98**	1.00						
Fe	**0.98**	0.18	**0.99**	**0.94**	1.00					
Ni	0.35	–0.04	0.29	0.27	0.33	1.00				
Cu	0.56	0.63	0.39	0.38	0.41	0.47	1.00			
Zn	–0.24	0.46	–0.09	–0.10	–0.11	–0.22	0.34	1.00		
Ga	0.55	0.77	0.25	0.24	0.27	0.09	**0.86**	0.65	1.00	
Se	**0.98**	0.29	**0.98**	**0.93**	**1.00**	0.39	**0.90**	–0.17	**0.86**	1.00

Notes for Tables 4a–e: If the number of data pairs was less than or equal to two, "nd" (= not determined) is shown.
If the number of pairs was 3–6, the coefficient value is shaded dark gray, indicating that these values are less well-defined.
Correlation coefficients with absolute values greater than 0.8 are in boldface, indicating a strong correlation.

Table 4b. Correlation coefficients: track C2115,20.

	S	Ca	Cr	Mn	Fe	Ni	Cu	Zn	Ga	Ge	Se
S	1.00										
Ca	–0.12	1.00									
Cr	–0.28	**0.82**	1.00								
Mn	–0.25	**0.80**	**0.97**	1.00							
Fe	–0.64	**0.83**	0.56	0.35	1.00						
Ni	**–0.84**	0.59	0.25	0.28	–0.03	1.00					
Cu	nd	nd	–0.37	–0.36	–0.16	–0.63	1.00				
Zn	nd	nd	0.23	0.32	–0.15	0.11	0.55	1.00			
Ga	nd	nd	–0.35	–0.33	–0.25	**–0.87**	0.53	0.32	1.00		
Ge	nd	nd	*–0.15*	*–0.22*	*0.14*	*0.67*	*–0.31*	*–0.43*	–0.49	1.00	
Se	nd	nd	***0.86***	***0.93***	–0.23	*0.70*	***–0.89***	*0.74*	***–0.90***	*–0.26*	1.00

Table 4c. Correlation coefficients: track C2115,21.

	S	Ca	Cr	Mn	Fe	Ni	Cu	Zn	Ga	Ge	Se
S	1.00										
Ca	**0.81**	1.00									
Cr	0.76	**0.83**	1.00								
Mn	**0.82**	**0.86**	**0.99**	1.00							
Fe	**0.98**	**0.90**	**0.84**	**0.89**	1.00						
Ni	**0.95**	**0.82**	0.70	0.75	**0.90**	1.00					
Cu	**0.93**	**0.82**	0.58	0.60	0.53	0.70	1.00				
Zn	**–0.86**	–0.14	–0.15	–0.17	–0.22	–0.18	0.23	1.00			
Ga	**0.80**	**0.87**	**0.87**	**0.88**	0.74	0.77	0.78	–0.13	1.00		
Ge	nd	nd	**–0.94**	**–0.97**	**–0.97**	–0.66	–0.70	–0.71	–0.72	1.00	
Se	nd	nd	0.71	0.77	0.90	0.81	0.73	0.16	0.74	–0.99	1.00

fragments. C2115,19 shows the most divergent Ca, Cr, and Zn compositions and is also the track with the most material along the entry trajectory (low terminal-particle to whole-track Fe ratio). C2027,48 is an interesting case. Recall that the abundance ranges were quite large for this track. However, we can see that the large range (particularly in Ca and Zn) is caused by the presence of a few fragments with very high abundances. The majority of the fragments actually fall in tight distributions, suggesting that the track is fairly homogeneous with rare outliers. Sulfur distributions are tight for C2115,19 and C2027,48, with most fragments near CI in the former and depleted in the latter. The tight distributions suggest sulfur-bearing components are ubiquitous and fine-grained, and/or sulfur is easily redistributed during capture. In general, many of the element distributions have a main peak accompanied by several fragments of grossly different composition and these outliers are typically at higher concentrations (likely to be components with the element at major concentration levels).

Other conclusions from the elemental distributions are:

1. The moderately volatile elements Cu, Zn, and Ga show the broadest compositional distributions.
2. Selenium distributions are typically tight and reasonably well-correlated with sulfur.

Table 4d. Correlation coefficients: track C2115,22.

	S	Ca	Cr	Mn	Fe	Ni	Cu	Zn	Ga	Ge	Se
S	1.00										
Ca	0.73	1.00									
Cr	**0.84**	**0.97**	1.00								
Mn	**0.91**	**0.81**	**0.94**	1.00							
Fe	**0.90**	**0.85**	**0.95**	**0.99**	1.00						
Ni	**1.00**	0.72	0.76	**0.82**	0.78	1.00					
Cu	0.59	0.12	0.32	0.40	0.34	0.76	1.00				
Zn	**0.94**	**0.80**	0.29	0.32	0.28	0.19	0.07	1.00			
Ga	**0.88**	0.79	**0.89**	**0.95**	**0.94**	**0.80**	0.39	0.33	1.00		
Ge	**0.98**	**1.00**	0.02	–0.05	–0.10	0.35	0.42	–0.07	–0.07	1.00	
Se	–0.38	–0.38	0.03	0.16	0.24	0.15	–0.08	–0.20	–0.08	–0.10	1.00

Table 4e. Correlation coefficients: track C2027,48.

	S	Ca	Cr	Mn	Fe	Ni	Cu	Zn	Ga
S	1.00								
Ca	–0.09	1.00							
Cr	–0.07	0.22	1.00						
Mn	0.32	0.63	**0.91**	1.00					
Fe	0.52	0.17	0.89	**0.99**	1.00				
Ni	–0.13	–0.06	0.20	0.14	0.22	1.00			
Cu	0.12	0.38	0.01	0.10	0.06	0.37	1.00		
Zn	0.10	0.55	–0.08	–0.07	–0.10	–0.26	0.23	1.00	
Ga	nd	0.57	**0.97**	**0.99**	**1.00**	0.06	–0.77	0.66	1.00

Table 5. Correlation coefficients for all particles.

	S	Ca	Cr	Mn	Fe	Ni	Cu	Zn	Ga	Ge	Se
S	1.00										
Ca	0.20	1.00									
Cr	0.40	0.50	1.00								
Mn	0.38	0.59	**0.91**	1.00							
Fe	0.49	0.48	**0.89**	**0.94**	1.00						
Ni	0.27	0.08	0.21	0.09	0.40	1.00					
Cu	0.21	0.17	0.10	0.15	0.18	0.71	1.00				
Zn	0.08	0.28	–0.04	0.04	–0.05	–0.09	0.25	1.00			
Ga	0.32	**0.84**	0.52	0.67	0.64	0.13	0.05	0.14	1.00		
Ge	0.17	**0.91**	–0.04	–0.09	–0.13	0.23	0.12	–0.10	–0.08	1.00	
Se	**0.83**	–0.03	0.26	0.15	0.29	0.22	0.34	–0.10	–0.01	–0.07	1.00

Note: Correlation coefficients with absolute values greater than 0.8 are in boldface indicating a strong correlation.

3. A strong correlation between track type and/or length and composition diversity is absent.
4. C2027,48 has the largest bulb and has the tightest compositional distributions. This could suggest a large fraction of fine-grained material that produced aggregate fragments of similar composition.
5. C2115,22 is the most bifurcated, suggesting multiple large crystals in the parent particle, which is consistent with the large number of Ni-depleted fragments.

The degree of heterogeneity is likely to be indicative of the grain size of the impacting parent particle. Those with grain sizes smaller than the typical in-track fragment size (comparable to the analysis spot size) are more likely to produce homogeneous abundance distributions, whereas those with grain sizes comparable to or greater than the in-track fragment size will produce more heterogeneous distributions. We therefore conclude that the grain size of the C2027,48 impactor was smaller than that of the other six tracks.

Other important characteristics of these samples are the correlations between elements, which can be useful in identifying phases present. Our individual fragment data is an ideal way to study such correlations and we approach this issue using correlation matrices. Tables 4a–e present correlation matrices for the five tracks with the most fragment analyses: C2115,19, C2115,20, C2115,21, C2115,22, and C2027,48. The number of data pairs (i.e., detectable concentrations) for each element pair was used to classify

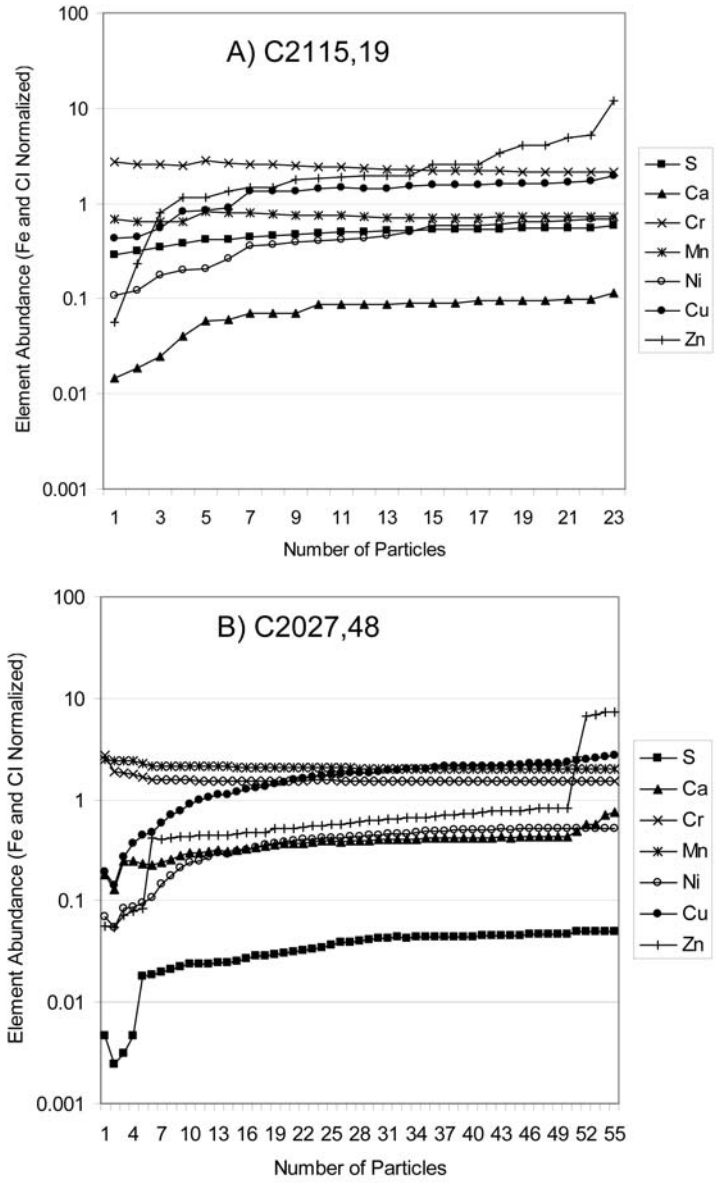

Fig. 8. Convergence profiles for element abundances for particles in tracks C2115,19 and C2027,48. The horizontal axis is the number of particles included in the abundance calculation with the particles arranged in decreasing order of Fe mass.

the correlation coefficient significance. If the number of pairs was less than or equal to two, "nd" (= not determined) was placed in that matrix cell. If the number of pairs was 3–6, the coefficient value was shaded dark gray, indicating that these values are less well-defined. Correlation coefficients with absolute value greater than 0.8 are in boldface, indicating a strong correlation. Below is a summary of the element correlation results for each track:

C2115,19: Iron, Cr, Mn, Se, and S are well-correlated, implying the presence of sulfides. Zinc, a chalcophilic element, is poorly correlated with these elements, suggesting that sulfide is not the principal Zn host phase. Gallium is correlated with Cu and, to a lesser extent, Ca and Zn. Since Ga shows similar chemical behavior to aluminum, it is likely that Ga resides in the Mg-Al silicate glass seen by TEM in fragments from this track. Another possibility is that Ga resides in olivine.

C2115,20: Calcium is correlated with Cr, Mn, and Fe, and Cr is well-correlated with Mn. These correlations are likely associated with pyroxene observed in this track. Nickel is not correlated with these elements, but is negatively correlated with Ga and S. This observation suggests that pentlandite is not the primary host of Ni. Nickel may be hosted in olivine.

C2115,21: As in C2115,20, calcium is correlated with Cr, Mn, Fe, Ni, Cu. Chromium, Mn, Fe, and Ni are correlated. Surprisingly, Ga is associated with all elements except Zn and is probably in glass.

C2115,22: Chromium, Mn, Fe, (Ni), and Ga are correlated and again not with Zn.

C2027,48: The only strong correlations are between Fe, Cr, and Mn. Nickel is not correlated strongly with them or any other elements.

In addition, a correlation matrix was produced for all 156 fragments analyzed in the seven tracks to increase the number of couples (Table 5). The strongest correlations were between S and Se, Ca with Ga and Ge, and Cr with Mn and Fe. The Cr-Mn-Fe association was found in all tracks and attributable to pyroxene. The S-Se association indicates sulfides are the selenium host. The Ca-Ga association was weak in the individual tracks but comes out strongly when considering the entire population. If Ga is hosted by the Mg-Al glass, the association with Ca suggests most of the Ca in the tracks is also hosted by the glass. The apparent inclusion of Ge with this association implies it is largely in the glass as well. Nickel is not strongly correlated with any of the detected elements including Fe, where there is only a moderate association. Nickel's strongest association is with Cu and the correlation with S is weak. Nickel is therefore probably predominately hosted by olivine.

It is remarkable that the elemental correlations among the particle tracks are so dissimilar (Table 4). This situation confirms the distinct nature of the individual impactors. In particular, it provides evidence for the high degree of mineralogical diversity among the impactors.

The large variation in fragment abundances (Tables 3a–g) raises the question about how well the whole track abundance patterns (Figs. 4a–g), produced by fragment elemental mass summation, are constrained. One way to evaluate this is to compare whole-track abundance patterns as fragment elemental masses are summed one fragment at a time. Such an evaluation will show how many analyses are required to approach compositional convergence. Convergence plots of this type are shown in Figs. 8a and 8b for tracks C2115,19 and C2027,48. The horizontal axis is the number of fragments included in the abundance calculation with the fragments arranged in decreasing order of Fe mass. Most of these curves are very well-behaved, converging after approximately 10 fragment analyses. Zinc is an exception, where it is clear that some low Fe fragments have significant fractions of the total Zn in the tracks. This is evidenced by the continually rising Zn profile for C2115,19 and is particularly pronounced for C2027,48, where a step in the convergence profile is observed. This suggests that the Zn abundance may be underestimated due to the focusing of our data collection on fragments that appear as hot-spots in Fe maps, although prominent fragments on other elemental maps were analyzed in some cases. One question is whether the "high Zn–low Fe mass" fragments are cometary or aerogel contaminants that unfortuitously occurred near a track. The answer to this question is not known with certainty at this time. Zinc-rich contaminants are known to occur in aerogel, but our analysis of these indicates they are not associated with other rock-forming elements. Thus, the association of these high-Zn fragments with other elements argues in favor of a cometary origin.

SUMMARY AND CONCLUSIONS

Seven cometary dust particle tracks in Stardust aerogel were studied using synchrotron X-ray fluorescence methods at the NSLS and APS. Elemental maps were produced for each of the tracks and elemental abundances for 156 individual fragments within these tracks were determined. Whole-track elemental abundances were inferred by summing the elemental masses for the fragments in each track and scaling by the ratio of total Fe in the map and total Fe in the fragments. In general, whole track and terminal particle abundances are dissimilar. The total Fe masses ranged from 4 to 2200 pg, corresponding to impactors in the 2.7 to 22 μm size range if chondritic. The resulting whole-track elemental abundances show diverse patterns that are generally chondritic (i.e., within a factor of 3 of CI abundances) with some exceptions, notably depletions in S and enrichments in the moderately volatile elements Cu, Zn, and Ga. Enrichments in large ion lithophile elements relative to Fe were observed in one track.

A statistical treatment of the in-track fragment chemical abundances using correlation matrices provided information on the heterogeneity, grain size, and element correlations of the Wild 2 cometary material. Element correlation plots showed that the large abundance ranges observed for the fragments are often due to a combination of relatively tight abundance distributions around the CI composition with a few additional fragments at much higher (or much lower) abundance. The breadth of these distributions could be used to infer semi-quantitatively the grain size of the impactor components relative to the analytical beam size of a few micrometers. Correlation matrices showed several strong elemental correlations, notably selenium associated with sulfides, ubiquitous correlation of the first row transition metals Cr, Mn, and Fe attributed to the presence of pyroxene, and enrichments of Ga associated with Ca, likely affiliated with Mg-Al glass. Compositional convergence data showed that typically the analysis of ~10 fragments was needed to reach a convergent whole track abundance. Zinc was an exception, showing non-convergent profiles and steps due to the presence of rare, high-Zn fragments.

Acknowledgments—Portions of this work were performed at GeoSoilEnviroCARS (Sector 13), Advanced Photon Source (APS), Argonne National Laboratory. GeoSoilEnviroCARS is supported by the National Science Foundation—Earth Sciences (EAR-0622171), and Department of Energy—Geosciences (DE-FG02-94ER14466). Use of the Advanced Photon Source was supported by the U. S. Department of Energy, Office of Science, Office of Basic Energy Sciences, under contract no. DE-AC02-06CH11357. Portions of this

work were performed at Beamline X26A, National Synchrotron Light Source (NSLS), Brookhaven National Laboratory. X26A is supported by the Department of Energy (DOE)—Geosciences (DE-FG02-92ER14244 to The University of Chicago—CARS) and DOE—Office of Biological and Environmental Research, Environmental Remediation Sciences Div. (DE-FC09-96-SR18546 to the University of Georgia). Use of the NSLS was supported by DOE under contract no. DE-AC02-98CH10886. This work benefited from an equipment grant from the NASA-Sample Return Laboratory Instrumentations and Data Analysis Program (SRLIDAP; G. Flynn, SUNY-Plattsburgh, PI). We also wish to thank the reviewers of this manuscript for their valuable comments.

Editorial Handling—Dr. Donald Brownlee

REFERENCES

Anders E. and Grevesse N. 1989. Abundances of the elements: meteoric and solar. *Geochimica et Cosmochimica Acta* 53: 197–214.

Chi M., Ishii H., Dai Z. R., Toppani A., Joswiak D. J., Leroux H., Zolensky M., Keller L. P., Browning N. D., and Bradley J. P. 2007. Does comet Wild 2 contain GEMS (abstract #2010)? 38th Lunar and Planetary Science Conference. CD-ROM.

Criss J. W. 1977. NRLXRF—Cosmic program #DOD-00065. U.S. Naval Research Laboratory.

Eng P. J., Newville M., Rivers M. L., and Sutton S. R. 1998. Dynamically figured Kirkpatrick-Baez micro-focusing optics. In *X-ray microfocusing: Applications and technique*, edited by McNulty I. Bellingham, Washington: SPIE Proc. 3449:145–156.

Eng P. J., Rivers M. L., Yang B. X., and Schildkamp W. 1995. Microfocusing 4-keV to 65-keV X-rays with bent Kirkpatrick-Baez mirrors. *Proceedings of SPIE* 2516:41–51.

Flynn G. J. and Durda D. D. 2004. Chemical and mineralogical size segregation in the impact disruption of inhomogeneous, anhydrous meteorites. *Planetary and Space Science* 52:129–1140.

Flynn G. J., Bajt S., Sutton S. R., Zolensky M. E., Thomas K. L., and Keller L. P. 1996. The abundance pattern of elements having low nebular condensation temperatures in interplanetary dust particles: Evidence for a new chemical type of chondritic material. In *Physics, chemistry, and dynamics of interplanetary dust,* edited by Gustafson B. A. S. and Hanner M. S. San Francisco: Astronomical Society of the Pacific. pp. 291–294.

Flynn G. J. and Sutton S. R. 1990 Synchrotron X-ray fluorescence analyses of stratospheric cosmic dust—New results for chondritic and low-nickel particles. Proceedings, 20th Lunar and Planetary Science Conference. pp. 335–342.

Flynn G. J., Bleuet P., Borg J., Bradley J., Brenker F., Brennan S., Bridges J., Brownlee D. E., Bullock E., Clark B. C., Dai Z. R., Daghlian C., Djouadi Z., Fakra S., Ferroir T., Floss C., Franchi I., Gainsforth Z., Gallien J.-P., Gillet Ph., Grant P. G., Graham G. A., Green S., Grossemy F., Heck P., Herzog G. F., Hoppe P., Hörz F., Huth J., Ignatyev K., Ishii H., Joswiak D., Kearsley A. T., Khodja H., Lanzirotti A., Leitner J., Lemelle L., Leroux H., Luening K., MacPherson G., Marhas K., Marcus M., Matrajt G., Nakamura T., Nakano T., Newville M., Papanastassiou D., Pianetta P., Rao W., Rietmeijer F., Rost D., Schwandt C., See T., Sheffield-Parker J., Simionovici A., Sitnitsky I., Snead C., Stadermann F., Stephan T., Stroud R., Susini J., Suzuki Y., Sutton S., Taylor S. R., Teslich N., Troadec D., Tsou P., Tsuchiyama A., Uesugi K., Westphal A., Wozniakiewicz P., Vicenzi E., Vincze L., and Zolensky M. E. 2006. Elemental compositions of comet 81P/Wild 2 samples collected by Stardust. *Science* 314:1731–1735.

Hill V., Roy R., and Osborn E. 1952. The system alumina-gallia-water. *Journal of the American Ceramic Society* 35:135–142.

Hörz F., Bastien R., Borg J., Bradley J. P., Bridges J. C., Brownlee D. E., Burchell M. J., Chi M., Cintala M., Dai Z., Djouadi Z., Dominguez G., Economou T. E., Fairey S., Floss C., Franchi I. A., Graham G. A., Green S. F., Heck P., Hoppe P., Huth J., Hope Ishii, Kearsley A. T., Kissel J., Leitner J., Leroux H., Marhas K., Messenger K., Schwandt C. S., See T. H., Snead C., Stadermann F. J., Stephan T., Rhonda Stroud, Teslich N., Trigo-Rodríguez J., Tuzzolino A. J., Troadec D., Tsou P., Warren J., Westphal A., Wozniakiewicz P., Wright I., and Zinner E. 2006. Impact features on Stardust: Implications for comet 81P/Wild 2 dust. *Science* 314:1716–1719.

Kirkpatrick P. and Baez A. V. 1948. Formation of optical images by X-rays. *Journal of the Optical Society of America* 38:766–774.

Lawrenchuck V. N. and Seruck V. S. 1966. About the relation between gallium and trivalent iron. *Acta Geologica Hungarica* 10:131–141.

Schramm L. S., Brownlee D. E., and Wheelock M. M. 1989. Major element composition of stratospheric micrometeorites. *Meteoritics* 24:99–112.

Sutton S. R., Newville M., Eng R., Rivers M., and Lanzirotti A. 2004. Mirror-based X-ray fluorescence microprobes at the Advanced Photon Source and the National Synchrotron Light Source. *Advances in X-ray Analysis* 76:76–84.

Sutton S. R., Bertsch P. M., Newville M., Rivers M., Lanzirotti A., and Eng P. 2002. Microfluorescence and microtomography analyses of heterogeneous earth and environmental materials. In *Applications of synchrotron radiation in low-temperature geochemistry and environmental science*, edited by Fenter P. A., Rivers M. L., Sturchio N. C., and Sutton S. R. Reviews in Mineralogy and Geochemistry, vol. 49. Washington, D.C.: Mineralogical Society of America. pp. 429–483.

Tsou P., Brownlee D. E., Sandford S. A., Hörz F., and Zolensky M. E. 2003. Wild 2 and interstellar sample collection and Earth return. *Journal of Geophysical Research* 108, doi:10.1029/2003JE002109.

Yang B. X., Rivers M. L., Schildkamp W., and Eng P. 1995. GeoCARS micro-focusing Kirkpatrick-Baez mirror bender development. *Review of Scientific Instruments* 66:2278–2280.

Zolensky M. E., Zega T., Yano H., Wirick S., Westphal A., Mike K., Iris Weber I., Warren J. L., Velbel M., Tsuchiyama A., Tsou P., Toppani A., Tomioka N., Tomeoka K., Teslich N., Taheri M., Susini J., Stroud R., Stephan T., Stadermann F., Snead C., Simon S., Simionovici A., See T., Robert F., Rietmeijer F., Rao W., Perronnet M., Papanastassiou D., Okudaira K., Ohsumi K., Ohnishi I., Nakamura-Messenger K., Nakamura T., Mostefaoui S., Mikouchi T., Meibom A., Matrajt G., Marcus M., Leroux H., Lemelle L., Le L., Lanzirotti A., Langenhorst F., Krot A., Keller L., Kearsley A., Joswiak D., Jacob D., Ishii H., Harvey R., Hagiya K., Grossman L., Grossman J., Graham G., Gounelle M., Gillet P., Genge M., Flynn G., Ferroir T., Fallon S., Ebel D., Dai Z.-R., Cordier P., Clark B., Chi M., Butterworth A., Brownlee D., Bridges J., Brennan S., Brearley A., Bradley J., Bleuet P., and Bland P., and Bastien R. 2006. Mineralogy and petrology of comet 81P/Wild 2 nucleus samples. *Science* 314: 1735–1739.